JOURNAL OF GEOPHYSICAL RESEARCH, VOL. 99, NO. B10, PAGES 19,947–19,974, OCTOBER 10, 1994

Effect of the brittle-ductile transition on the topography of compressive mountain belts on Earth and Venus

Charles A. Williams,[1] Chris Connors, F. A. Dahlen, Evelyn J. Price,[2] and John Suppe
Department of Geological and Geophysical Sciences, Princeton University, Princeton, New Jersey

Abstract. The Coulomb critical taper model has been very successful in explaining the large-scale topography of a number of terrestrial accretionary wedges; however, this model is limited to cases of purely brittle-frictional deformation. In this paper we extend the range of applicability of the critical taper model by explicitly including the effects of temperature-dependent ductile deformation. The new model includes temperature-dependent power law flow, an assumed velocity field, and linear thermal gradients in the atmosphere and within the crust. Flexural isostasy is also incorporated so that the decollement geometry is computed as a response to the applied load of the wedge material. We assume that ductile deformation within the decollement zone is controlled primarily by diffusion flow, whereas ductile deformation within the wedge itself is controlled by dislocation creep. The topographic profiles predicted by the model are very similar to those of a number of fold-and-thrust belts on both Earth and Venus. A typical wedge profile includes three distinctive topographic regions: a narrow taper toe, where both the wedge and the decollement zone deform in a brittle-frictional manner; a region of relatively steep slope, where the wedge base deforms ductilely and the decollement zone is still frictional; and a flat plateau region, where both the wedge base and the decollement zone are deforming by ductile flow. We have applied the model to two fold-and-thrust belts on Venus (Maxwell Montes and Uorsar Rupes) and to the Andes on Earth, and we find good agreement between observed and predicted topography using reasonable parameter values. The model accounts for the observed positive correlation between relief and elevation of Venusian fold-and-thrust belts on the basis of different thermal environments at different elevations. It is also able to explain the first-order differences between terrestrial and Venusian fold-and-thrust belts; fundamentally, this difference is due to a combination of the lower temperatures and the presence of water on Earth.

Introduction

Fold-and-thrust belts are commonly observed at the margins of compressive mountain belts and as submarine accretionary wedges on Earth, and recent analysis of data from the Magellan mission has revealed similar features on Venus [*Suppe and Connors*, 1992]. These structures display distinctive large-scale topographic signatures. Nearly all active fold-and-thrust belts exhibit a gently sloping toe region, which may be interpreted as a critical taper Coulomb wedge [*Davis et al.*, 1983]. Many of these structures are also characterized by a region of somewhat steeper slope followed by a relatively flat plateau. The latter two morphologies cannot be explained by a brittle-frictional Coulomb model. The essential premise of the Coulomb model is that deformation within a fold-and-thrust belt occurs only by brittle-frictional failure, an assumption that is obviously not true at high temperatures. To correct this limitation, we have extended the critical taper model to include the effects of temperature-dependent ductile creep. The topographic profiles predicted by this extended model bear a remarkable similarity to observed profiles. The steep slope and the plateau region are found to be related to the transition from brittle to ductile behavior within the base of the wedge and within the decollement zone, respectively.

The gross mechanics of the brittle-ductile critical taper model are the same as that of the Coulomb model: the wedge taper (decollement dip plus surface slope) is roughly proportional to the ratio of the applied basal shear stress to the strength of the material in the base of the wedge. The qualitative effect of the brittle-ductile transition is demonstrated in Figure 1. Near the toe of the wedge, deformation is dominated by frictional sliding and brittle failure. Both the wedge material and the decollement zone behave in a brittle-frictional manner, yielding the classic narrow taper wedge shape described by the critical taper Coulomb model (zone I). At greater depths and higher temperatures, the base of the wedge deforms in a ductile rather than a brittle manner. This causes the ratio of applied shear stress to basal strength to decrease, resulting in a larger taper, and thus producing a steep surface slope (zone II). At still greater depths, the decollement zone also becomes ductile, reducing the ratio and causing the surface slope to flatten (zone III). This is precisely the morphology that we observe in many fold-and-thrust belts on both Earth and Venus, as seen in Figures 2a, 2b, 2c, and 2d. Figure 2a is a topographic profile across the eastern margin of the Andes near 21°S, and Figure 2b shows the topography of the Himalayas and Tibet near 85°E. Venusian fold-and-thrust belts reveal a similar topographic character, as demonstrated by Uorsar Rupes, a fold-and-thrust belt at the margin of the Itzpopalotl tessera plateau north of Freyja Montes (Figure 2c), and Maxwell Montes, a fold-and-

[1]Now at Lawrence Livermore National Laboratory, Livermore, California.

[2]Now at Scripps Institute of Oceanography, La Jolla, California.

Paper number 94JB01407
0148-0227/94/94JB-01407$05.00

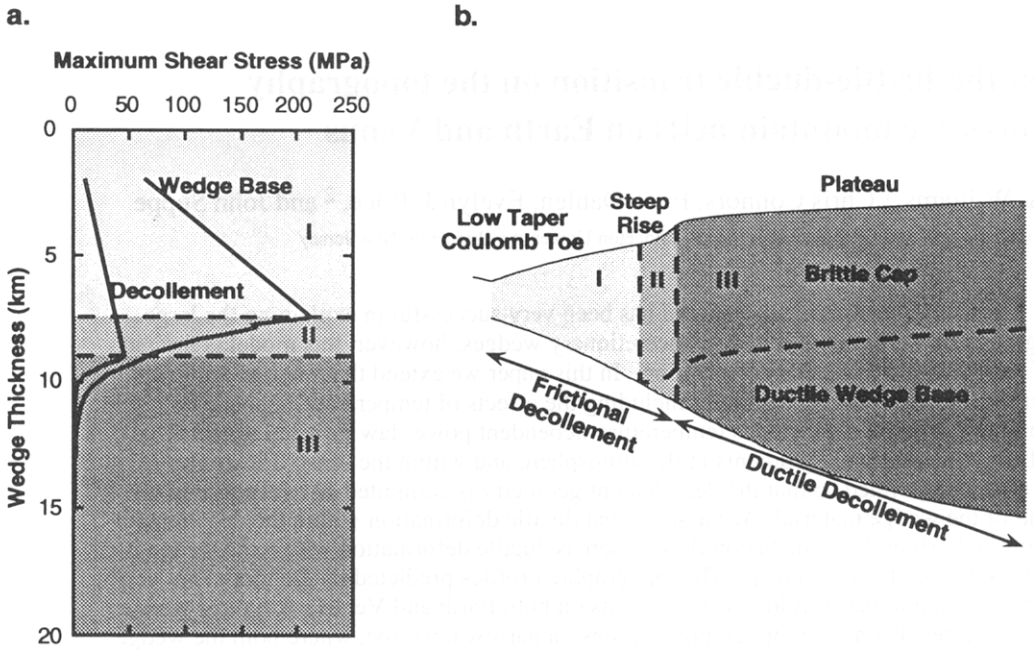

Figure 1. Representation of the brittle-ductile critical taper model. The wedge taper is controlled by the relative strengths of the wedge base and the decollement zone. In a typical configuration, the wedge is divided into three regions: a narrow taper toe, where both the decollement and the wedge base behave in a brittle-frictional manner (zone I); a steep rise, where the decollement is still frictional but the wedge base is ductile (zone II); and a flat plateau region, where both the wedge base and the decollement behave in a ductile manner (zone III). (a) The maximum shear stress in the wedge base and the decollement zone. The rightmost curve represents the strength of the wedge base. (b) The geometry of the wedge corresponding to the strength curve. The dashed line represents the brittle-ductile transition within the wedge.

thrust belt on the eastern margin of Lakshmi Planum in the northern latitudes of Venus (Figure 2d). Although the details differ, all of these regions display similar topographic profiles, consisting of a gently sloping toe, a steep rise, and a flat plateau. Owing to the irregular shape of the India-Eurasia collision zone and to the complex (and largely unknown) tectonic processes occurring there, it is unlikely that this area can be adequately represented by a simple two-dimensional model; however, the overall character of this region is in good agreement with the model predictions.

Many plateaus are characterized by high topography around their margins. This is observed on both Earth and Venus (see Figure 2) and is not accounted for by our model. On Earth, erosion may play an important role in the evolution of plateau margins. *Molnar and England* [1990] have shown how locally high topography may result from the incision of deep valleys through regions of high elevation. This causes isostatic uplift, thus increasing the elevations of the highest peaks, while leaving the mean elevation relatively unchanged. *Fielding et al.* [1994] have explained the high relief around the margins of the Tibetan Plateau as the result of fluvial dissection. Erosion is unlikely to be an important factor in the evolution of Venusian plateaus due to the absence of water, but other explanations are possible. For example, *Head* [1990] has proposed that the locally high topography at the margin of Uorsar Rupes is due to the imbrication of crustal slices. We are presently only able to account for the first-order characteristics of accretionary wedges, inasmuch as our model does not allow specifically for either erosion or laterally heterogeneous material properties within the wedge.

The critical taper concept is not new. Early analyses of this type include those of *Elliott* [1976] and *Chapple* [1978]. These models were later modified by *Davis et al.* [1983] and *Dahlen* [1984] to include brittle-frictional behavior. A related model, using plastic slip line theory and a von Mises yield criterion, was proposed by *Stockmal* [1983]. A Newtonian viscous wedge model has been developed by *Emmerman and Turcotte* [1983] and a similar model has been applied by *Vorder Bruegge and Fletcher* [1990] to overthrust zones on Venus. More recently, *Willett* [1992] has numerically modeled the dynamics of accretionary wedge deformation using a cohesionless Coulomb rheology. All of these models assume that the steady state wedge shape is controlled by the strength of the material composing the wedge, although the assumed rheology varies from model to model. It should be emphasized that the term "critical taper" applies to the long-term, steady state behavior of a wedge. If conditions change (for example, if subduction ceases or pore fluid pressure changes), the wedge will maintain the same taper as before, unless the change acts to push the wedge out of a stable state (see, for example, *Dahlen* [1984]), in which case the wedge will attain a new critical taper. Furthermore, it should be understood that a wedge is considered critical only macroscopically: heterogeneities and local failure may tend to push some interior regions out of a critical state.

The critical Coulomb model generally predicts a wedge characterized by a narrow, nearly constant taper and has found wide applicability to terrestrial accretionary wedges. The model has been successfully applied to regions such as Taiwan and Barbados, yielding excellent agreement between predicted and observed topography [*Davis et al.*, 1983; *Dahlen*, 1990]. Our present work represents an attempt to extend the applicability of the critical Coulomb model.

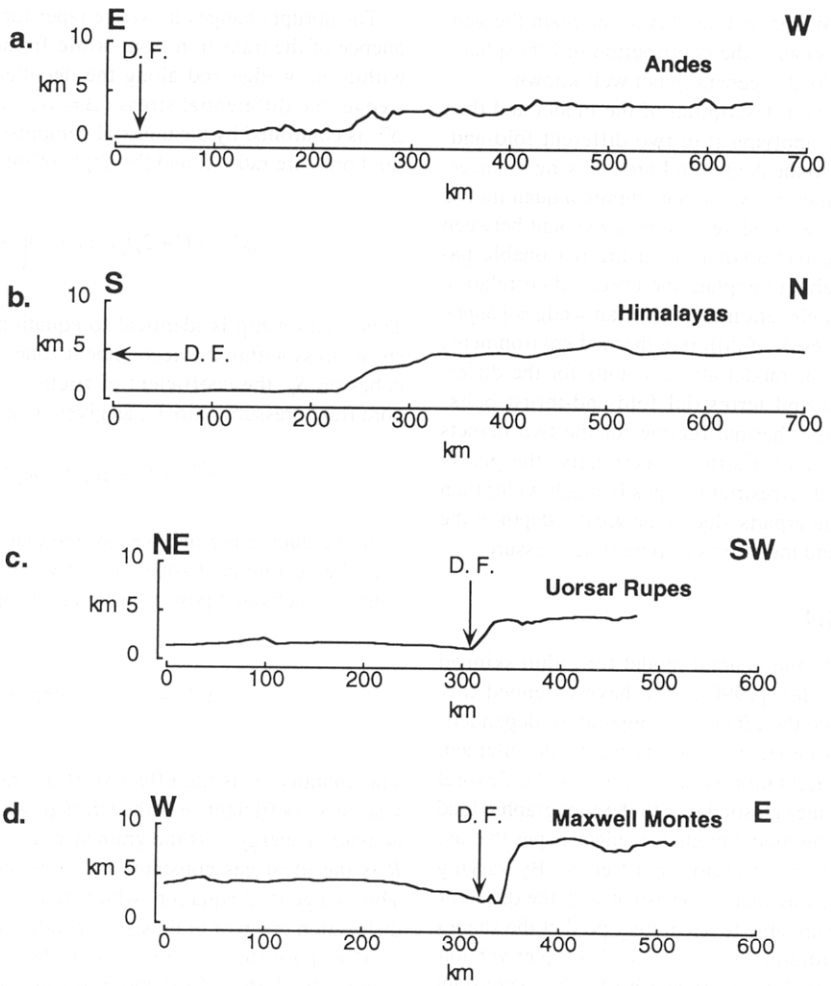

Figure 2. Topographic profiles across a number of compressive mountain belts. The vertical exaggeration in each case is 10:1. All of the belts demonstrate the characteristic features predicted by our model, consisting of a gently sloping toe, a steep rise, and a flat plateau. The deformation front (DF) is indicated by an arrow for each profile (for the Himalayas, the deformation front occurs outside the bounds of the figure). The important differences between the terrestrial examples (Figures 2a and 2b) and their Venusian counterparts (Figures 2c and 2d) are that the Venusian belts have a shorter toe region, and the rise is much more pronounced. (a) East-to-west profile of the Andes at 20.80°S (from the digital topographic data set of *Isacks* [1988]). (b) Approximately north-to-south profile of the Himalayas near 85°E [from *LePichon et al.*, 1992]. (c) Profile of Uorsar Rupes (from Magellan altimetry data). (d) Profile of Maxwell Montes (from Magellan altimetry data).

The primary difference between the model described here and other wedge models is that we explicitly include the effects of both brittle-frictional and ductile behavior. The distinctive features of the model, the relatively abrupt changes in slope, are due to the transition from brittle-frictional to ductile deformation. The other models listed above assume the same deformation mechanism throughout the wedge and therefore predict smoothly varying surface slopes. We should note that in a recent model, *Willett et al.* [1993] have been able to achieve steep slopes when new material is added to the rear of the wedge, rather than the toe, similar to the sandbox experiments of *Wang and Davis* [1992]. In their model, the taper attained by accreting material at the wedge toe represents the minimum critical taper, whereas the taper produced by adding material to the rear of the wedge represents the maximum critical taper [*Dahlen*, 1984]. They are thus able to produce a wedge with a narrow taper toe and a steep slope region without appealing to nonbrittle behavior. This model may prove useful in explaining wedge topography in regions where ductile behavior is relatively unimportant. We assume explicitly in the model to be described here that all the material that enters the wedge is accreted at the toe.

As a further refinement of the critical taper model, we have also incorporated flexural isostasy into our present model. The shape of the decollement zone is no longer specified a priori but is instead a result of the calculations. We believe that this results in a more realistic decollement zone geometry than the constant slope that is commonly assumed. For simplicity, we have assumed an elastic flexure model, although much of the lithosphere beneath the wedge is below the brittle-ductile transition. Although viscous flexure might be more appropriate, such added complexity is probably unwarranted for the present model, particularly since we are only interested in the steady state solution. Our flexure model also assumes a constant lithospheric thickness and thus does not take into account any additional loads due to

lithospheric thickening. We have done this to maintain the generality of the model and because the contribution of lithospheric thickening to the flexural load is generally not well-known.

In this paper, we present a description of the model and then demonstrate its utility by applying it to two different fold-and-thrust belts on Venus and to the Andes on Earth. Owing to uncertainties in the model parameters, we do not attempt a quantitative best fit analysis; however, we find very good agreement between observed topography and our predictions using reasonable parameter values. We are able to explain the observed correlation between wedge relief and elevation for Venusian wedges [*Suppe and Connors*, 1992] as a result of different thermal environments at different elevations. Our model also accounts for the differences between Venusian and terrestrial fold-and-thrust belts, based on differences in the thermal regime for the two planets and the presence of water on Earth. Specifically, the gently sloping frictional region of terrestrial wedges is much wider than that of their Venusian counterparts, due to the greater depth of the brittle-ductile transition and the effects of pore fluid pressure.

Critical Taper Model

The model is similar to the general model for a thin-skinned wedge described by *Dahlen* [1990]. We have extended this model to explicitly include the effects of temperature-dependent power law rheology, and rather than specifying the decollement orientation a priori, the orientation is determined by the flexural response of the planet's outer elastic layer to the topographic load of the wedge. The resulting model predicts wedge shapes that are typical of those observed on both Earth and Venus. By varying the model parameters in a way that is consistent with the different wedge environments, we are able to accurately predict the shapes of a number of different fold-and-thrust belts. A simpler version of this model, which utilizes local isostasy (or specifies a constant slope decollement) and does not include a strain rate dependency for viscous deformation, has been used by *Price et al.* [1992] to examine fold-and-thrust belts on Venus, and good agreement was found between observed and predicted topography. The incorporation of flexure into the model is crucial, because it allows the support of much greater surface slopes than would be possible with local isostasy. In earlier models, large surface slopes were only obtainable when the decollement geometry was fixed.

Here we provide a general description of our brittle-ductile critical taper model. The details of the mathematical derivation are given in Appendix A; we will make frequent reference to the appendix equations in this section.

The general wedge geometry is shown in Figure 3. Figure 3a depicts the geometry used in the derivation of the critical taper equation (A8), with axes locally aligned with the surface of the wedge. Figure 3b represents the geometry used in computing the wedge shape, where we ignore the slight variable tilt of the x and z axes. The wedge shape is described by the dip of the decollement β and the surface slope α. The wedge taper is equal to the sum of the decollement dip and the surface slope, $\alpha + \beta$. In the initial model, the decollement dip is regarded as a specified function of the horizontal distance x; we will later assume that β is controlled by flexural isostasy. The wedge thickness is h, and the thickness of the material at the toe of the wedge is h_0. The density of the wedge material is ρ_c, and the density of the overlying fluid or dense gas is ρ_f (in general, for a subaerial wedge on Earth, $\rho_f = \rho_{air} \approx 0$). The decollement zone has thickness δ, and the frictional and ductile properties within this zone are generally different from the corresponding properties within the wedge.

The abrupt changes in wedge taper for our model are a consequence of the transition from brittle-frictional to ductile behavior within the wedge and along the decollement zone. Within the wedge, the differential stress ($\Delta = \sigma_3 - \sigma_1$) in the brittle regime Δ^{brit} is controlled by the uniaxial compressive strength C, the pore fluid pressure ratio λ, and the angle of internal friction ϕ:

$$\Delta^{brit} \approx C + 2\rho_c g z(1-\lambda)\left(\frac{\sin\phi}{1-\sin\phi}\right). \quad (1)$$

This relationship is identical to equation (A13). The frictional shear stress within the decollement zone τ_d^{fric} is controlled by the cohesion S_d, the coefficient of friction μ_d, and the decollement pore fluid pressure ratio λ_d, as given here and in equation (A15):

$$\tau_d^{fric} = S_d + \mu_d(1-\lambda_d)\rho_c g h. \quad (2)$$

In the ductile regime, we assume that the differential stress in both the decollement zone and the wedge base is controlled by a thermally activated power law relationship, as in equation (A17):

$$\Delta^{duct} = \left(\frac{\dot{\varepsilon} s^p}{A}\right)^{\frac{1}{n}} \exp\left(\frac{Q}{nRT}\right). \quad (3)$$

The quantity $\dot{\varepsilon}$ is the effective strain rate, A is the generalized viscosity coefficient, n is the stress power law exponent, Q is the activation energy, s is the grain size, p is the grain size exponent, R is the ideal gas constant, and T is the absolute temperature. This is a general equation, which includes the possibility of either dislocation creep or grain size dependent diffusion creep.

Most published results on rock rheology, such as those summarized by *Kirby* [1983] and *Kirby and Kronenberg* [1987], have been concerned primarily with dislocation creep mechanisms, in which the strain rate is relatively insensitive to grain size and is instead proportional to a power of the differential stress. Several recent studies, however, have concentrated on the diffusion creep regime. Analysis of the deformation of synthetic olivine aggregates by *Karato et al.* [1986] have shown that diffusion creep is enhanced by lower stress, smaller grain size, and presence of water. Unlike dislocation creep, diffusion creep is sensitive to grain size and is linearly proportional to the applied differential stress. For the case of synthetic olivine aggregates, *Karato et al.* [1986] found the stress exponent n to be equal to one, and they found the grain size exponent p to be 2 for "dry" olivine aggregates and 3 for "wet" aggregates. In the dislocation creep regime, they found the grain size exponent to be zero, and the stress exponent to be 3.5 for "dry" samples and 3.0 for "wet" samples.

Rutter and Brodie [1988] have proposed that the most significant tectonic displacements may occur across major, localized shear zones. Owing to dynamic recrystallization, the grain size within the shear zone is reduced, thus moving the deformation mechanism from the dislocation creep to the diffusion creep regime, and thereby weakening the material within the shear zone. Although quantitative results exist so far only for olivine aggregates, *Tullis and Yund* [1991] have found experimental evidence for diffusion creep in feldspar aggregates. In their experiments on albite aggregates of 2-10 μm grain size, diffusion flow was only observed when the sample contained ~0.9 wt % water; however, with continued reduction in grain size, it is likely that diffusion flow could also occur in "dry" aggregates (J. Tullis, personal communication, 1992).

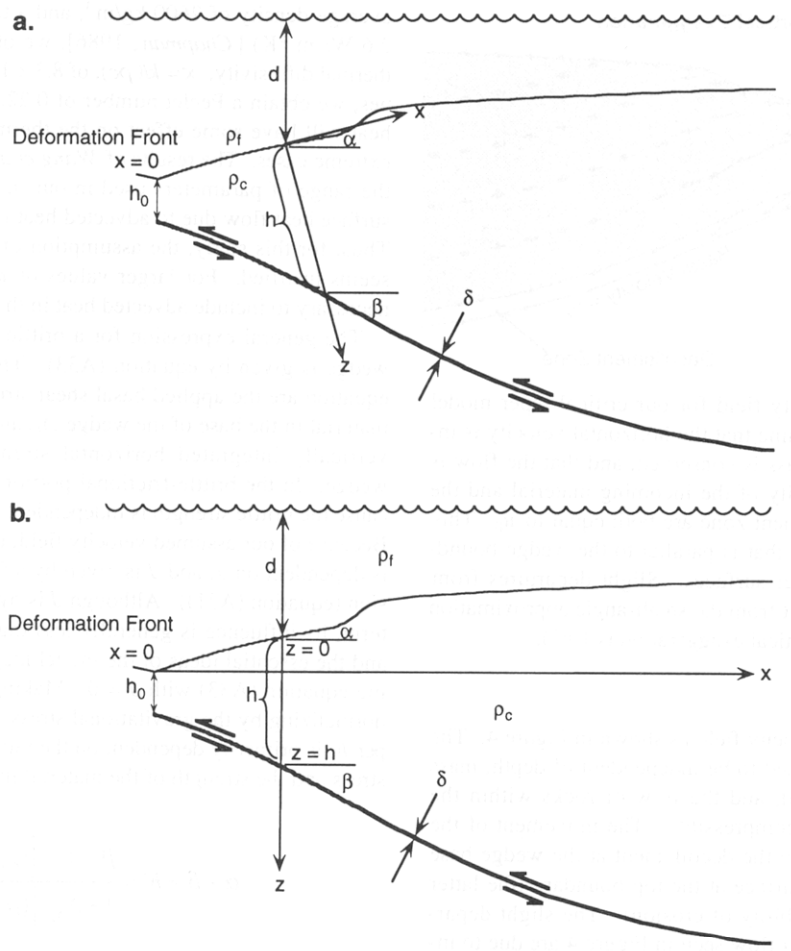

Figure 3. Schematic cross section of a thin-skinned critical taper wedge, adapted from *Dahlen* [1990]. The variables are d, the depth of the overlying fluid or dense gas; ρ_f, the density of the fluid or dense gas; ρ_c, the density of the material composing the wedge; h_0, the wedge thickness at the deformation front; h, the thickness within the wedge interior; α, the surface slope; β, the decollement dip; and δ, the thickness of the decollement zone. (a) In the derivation of our critical taper model, the local x axis is aligned parallel with the upper surface of the wedge and the local z axis is perpendicular to the upper surface. (b) In applying the brittle-ductile critical taper equation (equation (A33)) it is permissible to employ horizontal and vertical x and z axes, thus ignoring the slight tilt of the upper surface. The horizontal distance from the deformation front is thus given by x, while z represents the vertical distance below the upper wedge surface.

These rheological studies have important implications for our model. In a localized shear zone, such as the decollement zone of our model, grain size would decrease, and diffusion creep would likely be the dominant ductile deformational mechanism. Thus, even though the strain rate within the decollement zone is greater than within the wedge, its ductile strength can still be less than that of the wedge because of the weakening effects of dynamic recrystallization. This is an important attribute because if the decollement zone were stronger than the wedge, the fault would change its position and move into the weaker zone. Dynamic recrystallization offers a simple mechanism for maintaining a "steady state" shear zone over an extended period of time.

We should emphasize that our model results are not dependent on the specific deformation mechanisms that we use. The only requirement of our model is that the decollement zone remain weaker than the wedge base at all depths. Although the evidence presented above lends some support to the idea of a dislocation creep mechanism in the wedge itself and a diffusion flow mechanism within the decollement zone, the actual situation is probably more complex. It is possible, for instance, that the decollement zone may be weakened by dynamic recrystallization, even without a transition to the diffusion flow regime [*Tullis and Yund*, 1985], or by one of several other strain weakening mechanisms (see, for example, the review by *Evans and Dresen* [1991]). We should also caution against a literal interpretation of the parameters used in our rheological models. There are large uncertainties associated with these parameters and with the extrapolation of the parameter values to geologic environments [*Paterson*, 1987; *Strehlau and Meissner*, 1987; *Rutter and Brodie*, 1991]. Thus, although we employ laboratory results on rock rheology in our models of terrestrial and Venusian wedges, it is quite possible that a different set of parameters might be more suitable.

The model requires us to specify the absolute temperature T and the effective strain rate $\dot{\varepsilon}$. For simplicity, we assume linear temperature gradients in the atmosphere and within the planet's surface, given by ∇T_A and ∇T, respectively. We also specify the surface temperature at the wedge toe T_0, yielding equation (A19) as the differential stress for viscous flow. To obtain the effective

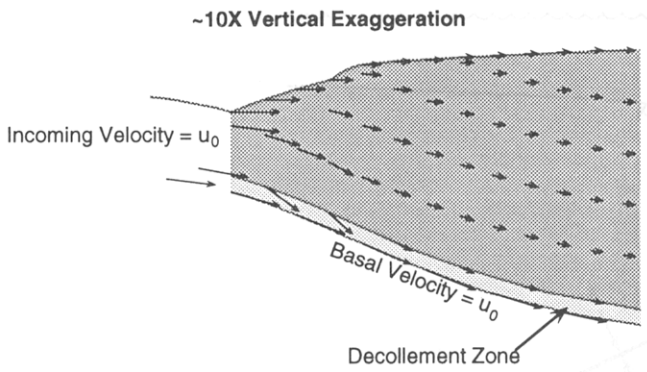

Figure 4. Assumed velocity field for our critical taper model (equations (A20)). We assume that the horizontal velocity is independent of depth, that mass is conserved, and that the flow is incompressible. The velocity of the incoming material and the velocity below the decollement zone are both equal to u_0. This should give a velocity field that is parallel to the wedge boundaries at the upper and lower surfaces. Slight departures from boundary-parallel flow result from the small-angle approximation used in our calculations (vertical exaggeration is 10:1).

strain rate, we assume a velocity field as shown in Figure 4. The horizontal velocity is assumed to be independent of depth, mass is assumed to be conserved, and the flow of rocks within the wedge is assumed to be incompressible. The movement of the wedge material is parallel to the decollement at the wedge base and parallel to the wedge surface at the top boundary (the latter condition ignores the possibility of erosion). The slight departures from boundary-parallel flow seen in Figure 4 are due to inaccuracies in the small-angle approximation (note that the vertical exaggeration is 10x). At the bottom of the decollement zone, the velocity is simply equal to the convergence velocity u_0. Given the velocity field (equations (A20)), it is then possible to determine the effective strain rate in the wedge (equation (A23)) and within the decollement zone (equation (A27)). The ductile strength within the wedge is thus given by equation (A24) and the basal shear traction in the ductile regime is given by equation (A28). Both relationships involve a preexponential factor that includes the strain rate dependence (related to geometry) and the grain size dependence, as well as an exponential factor to account for the temperature dependence.

Our assumed thermal model is an obvious simplification, since it does not include advective heat transfer within the wedge. To determine what effect this might have on our results, we need to estimate the degree to which advective heat perturbs a linear temperature gradient. The efficiency of advective heat transfer within an accretionary wedge with our assumed velocity field may be characterized by the Peclet number [*Wang et al.*, 1993],

$$Pe = \frac{u_0 h_0 \tan(\alpha+\beta)}{\kappa}, \tag{4}$$

where κ is the average thermal diffusivity of the wedge material. If $Pe \ll 1$, the thermal field reequilibrates more quickly than the wedge thickening perturbs it, and the effect of advective heat transfer is negligible. For the models presented in this paper, the maximum product of u_0 and h_0 is approximately 6.3×10^{-7} m^2/s, and the maximum wedge taper for our models is about 16°. Assuming a specific heat c of 1200 J/(kg °K) [*Oxburgh*, 1980], an average density of 2600 kg/m^3, and a thermal conductivity k of 2.6 W/(m °K) [*Chapman*, 1986], we obtain an estimate for the thermal diffusivity, $\kappa = k/(\rho c)$, of 8.3×10^{-7} m^2/s. With these values, we obtain a Peclet number of 0.22, indicating that advected heat will have some effect on the thermal gradients in the most extreme cases. The results of *Wang et al.* [1993] indicate that for the range of parameters used in our models, the perturbation of surface heat flow due to advected heat is no more than about 5%. Thus, for this study, the assumption of linear thermal gradients seems justified. For larger values of u_0 and h_0, it might prove necessary to include advected heat in the thermal model.

The general expression for a brittle-ductile critically tapered wedge is given by equation (A33). The important terms in the equation are the applied basal shear stress τ_d, the strength of the material in the base of the wedge Δ_h, and the term J, which is the vertically integrated horizontal strength gradient within the wedge. In the brittle-frictional portion of the wedge, $J = 0$ because the brittle strength is independent of x (see equation (A13)). Because of our assumed velocity field, the ductile wedge strength is dependent on x, and J is given by a fairly complicated expression (equation (A31)). Although J is by no means a second-order term, its influence is generally less than that of either τ_d or Δ_h, and the essential ideas of the model may be grasped by considering equation (A33) with $J = 0$. Making this approximation, and normalizing by the gravitational stress, we see that the wedge taper h' is primarily dependent on the ratio between the basal shear stress and the strength of the material in the wedge base:

$$\alpha+\beta \approx h' \approx \frac{\beta + \tau_d \Big/ \left[(\rho_c - \rho_f) g h\right]}{1 + \Delta_h \Big/ \left[(\rho_c - \rho_f) g h\right]}. \tag{5}$$

In general, the decollement dip β changes fairly slowly with respect to the other parameters, unless the effective elastic thickness is very small. Abrupt changes in the wedge taper and the surface slope, as exhibited in Figure 2, are therefore produced by abrupt changes in either τ_d or Δ_h. We believe that such changes can occur when the dominant deformational mechanism changes from brittle-frictional to ductile in the wedge base or within the decollement zone. If the wedge base becomes ductile, we would expect an increase in surface slope; if the decollement zone becomes ductile, the surface slope should decrease.

In equations (A33) and (5), we can see that the decollement dip β appears on the right-hand side of the equation. As mentioned before, β can be any specified function of x, and one method of solving the critical taper equation would be to completely specify β before solving the problem. This would be a reasonable approach in cases where the decollement geometry is well-determined by seismic or other data; however, this is generally not the case, particularly on Venus, where we have no direct information on subsurface structure. For that reason, we chose to make the decollement dip a product of the calculations. We assume that decollement position is controlled by flexural isostasy. We should emphasize that the concept of an effective elastic thickness is not related to any specific mechanical discontinuity within the planet but instead represents an integrated average of the lithosphere beneath the wedge over geologic timescales.

The assumed geometry for our flexure model is shown in Figure 5. A reference column at a point x_r, far away from the deformed portion of the wedge, is balanced against a column through an arbitrary position within the wedge. The depth of overlying water or dense atmosphere is $d(x)$, and its density is ρ_f.

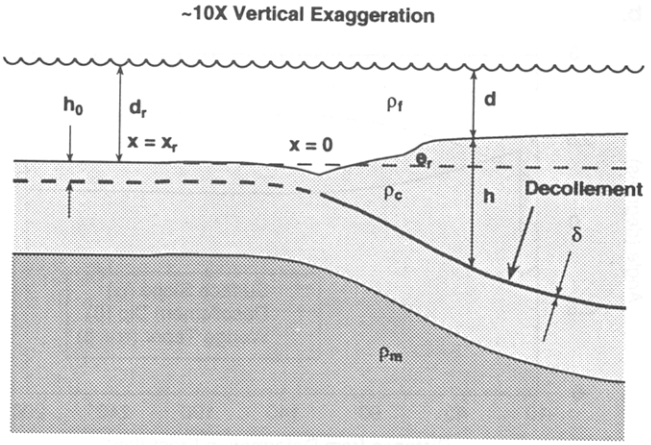

Figure 5. Assumed geometry for computing the flexural response of the lithosphere to the load of an accretionary wedge. Loads are computed by comparing a reference section at $x = x_r$ to sections within the wedge (equation (A36)). The depth of the overlying water or dense gas is d, and the thickness of the incoming material is h_0. Within the wedge the thickness is given by h. Below the decollement zone is a layer of constant thickness and unspecified density to allow for crustal material between the decollement and the top of the mantle.

The wedge material, with density ρ_c, is assumed to have constant thickness h_0 from x_r to the deformation front at $x = 0$ and thickness $h(x)$ within the wedge. The decollement zone is assumed to have constant thickness δ across the entire region of interest, and its density is unspecified. Beneath the decollement zone is a zone of constant thickness and unspecified density. The presence of this zone does not affect the model; we have shown it in Figure 5 only to allow for crustal material between the decollement and the top of the mantle. Beneath this layer is mantle material of density ρ_m. By balancing the two columns, we obtain the total load (equation (A38)) and compute the flexural response of the lithosphere to the load of the wedge material (equation (A46)).

Model Characteristics

This section describes the general characteristics of the brittle-ductile critical taper model. A more rigorous analysis of the influence of the various model parameters on the observable wedge characteristics may be found in Appendix B. In addition, Table B1b provides a brief description of each of the model parameters used in this study.

Importance of Ductile Behavior

To understand the characteristics of a brittle-ductile critical taper model, we will first look at the case of a purely frictional model. For this model, we used parameter values similar to those used in our model of the Andes (Table 1), with the following exceptions: $\mu_d(1 - \lambda_d) = 0.2$, $(1 - \lambda_h)\sin\phi_h/(1 - \sin\phi_h) = 1.06$, $\log_{10}A = -3.0$ (A in units of $MPa^{-n}\ s^{-1}$), and $\nabla T = \nabla T_A = 0°C/km$ (this causes the wedge to remain frictional). The geometry of the model is shown in Figure 6a, the slopes are shown in Figure 6b, and the strength and strain rate curves are shown in Figures 6c and 6d, respectively. The important point to note about this model is that the taper never decreases but instead approaches a limiting value at distances far from the wedge toe (see Figures 6a and 6b). We obtain a wedge of nearly constant taper, similar to previous models by *Davis et al.* [1983], *Dahlen* [1984], and others. The strength curves (Figure 6c) are straight lines, representing the brittle strength of the wedge base and the frictional sliding strength of the decollement zone. Note that the vertical axis of the strength curve is the wedge thickness h rather than depth. This is because the curves indicate the strength along the base of the wedge (solid line in Figure 6c) and along the decollement zone (dashed line) rather than representing the strength within a vertical section. The limiting taper may be deduced from equations (A13), (A15), and (A16). If we assume that $\rho_f = \lambda_h = \lambda_d = 0$, as we have done in Figure 6, the taper as $h \to \infty$ is

$$h' \approx \frac{\beta + \mu_d}{1 + 2\sin\phi_h/(1 - \sin\phi_h)}. \tag{6}$$

The term μ_d controls the slope of the decollement strength curve and the term $\sin\phi_h/(1 - \sin\phi_h)$ controls the slope of the wedge base strength curve. Note that the first term is always less than the second as long as $\phi_d = \tan^{-1}\mu_d$ is less than ϕ_h, thus ensuring that the frictional strength of the decollement is always less than that of the wedge base. The situation is altered slightly for a wedge with pore fluids ($\lambda_h, \lambda_d \neq 0$) or a submarine wedge ($\rho_f \neq 0$), but the results are similar.

The strain rate curves (Figure 6d) do not affect the rheology of a purely Coulomb model, since brittle-frictional strength is unrelated to the strain rate, but they serve to show the general strain rate characteristics of our assumed velocity model. These characteristics may be inferred qualitatively from Figure 4. The strain rate in the wedge base (solid line in Figure 6d) is a maximum at the toe and decreases with distance along the decollement, while the strain rate within the decollement zone is a minimum at the toe of the wedge and increases quickly to its maximum value a short distance into the wedge.

Clearly, a wedge cannot have infinite thickness, as would occur in our Coulomb model if the x axis were extended to infinity. This situation is rectified when ductile behavior is included in the model, as seen in Figure 7. For this model, we used the same parameters as for Figure 6, except that $\nabla T = 25°C/km$ and $\nabla T_A = 8°C/km$. The wedge geometry in Figure 7a displays the characteristic features described in the Introduction, including a narrow taper cohesive toe, a steep rise, and a relatively flat crest. Also shown in this plot are the brittle-ductile transition within the wedge (dashed line in Figure 7a) and the frictional-ductile transition on the decollement, shown with a cross. Note that the brittle-ductile transition within the wedge is closer to the surface toward the back of the wedge. This is because the strain rate in the wedge (solid line in Figure 7d) decreases as the wedge becomes thicker and the taper decreases (see equation (A23)). The small region between the point where the wedge brittle-ductile transition intersects the decollement and the point where the decollement becomes ductile corresponds to the region of steep surface slope. Note that the sudden increase in wedge taper is reflected primarily in the surface slope rather than in the dip of the decollement (Figure 7b): the flexural response of the elastic layer below the decollement prevents abrupt changes in the decollement dip. The changes in wedge taper may be understood by examining the strengths of the wedge base and the decollement, as shown in Figure 7c. The brittle-ductile and frictional-ductile transitions correspond to the two regions of greatest strength. Between these two peaks, the strength of the wedge base is decreasing, whereas the strength of the decollement is still increasing. Thus, according to equations (4) and (A33), the wedge taper should increase. When the decollement becomes ductile and be-

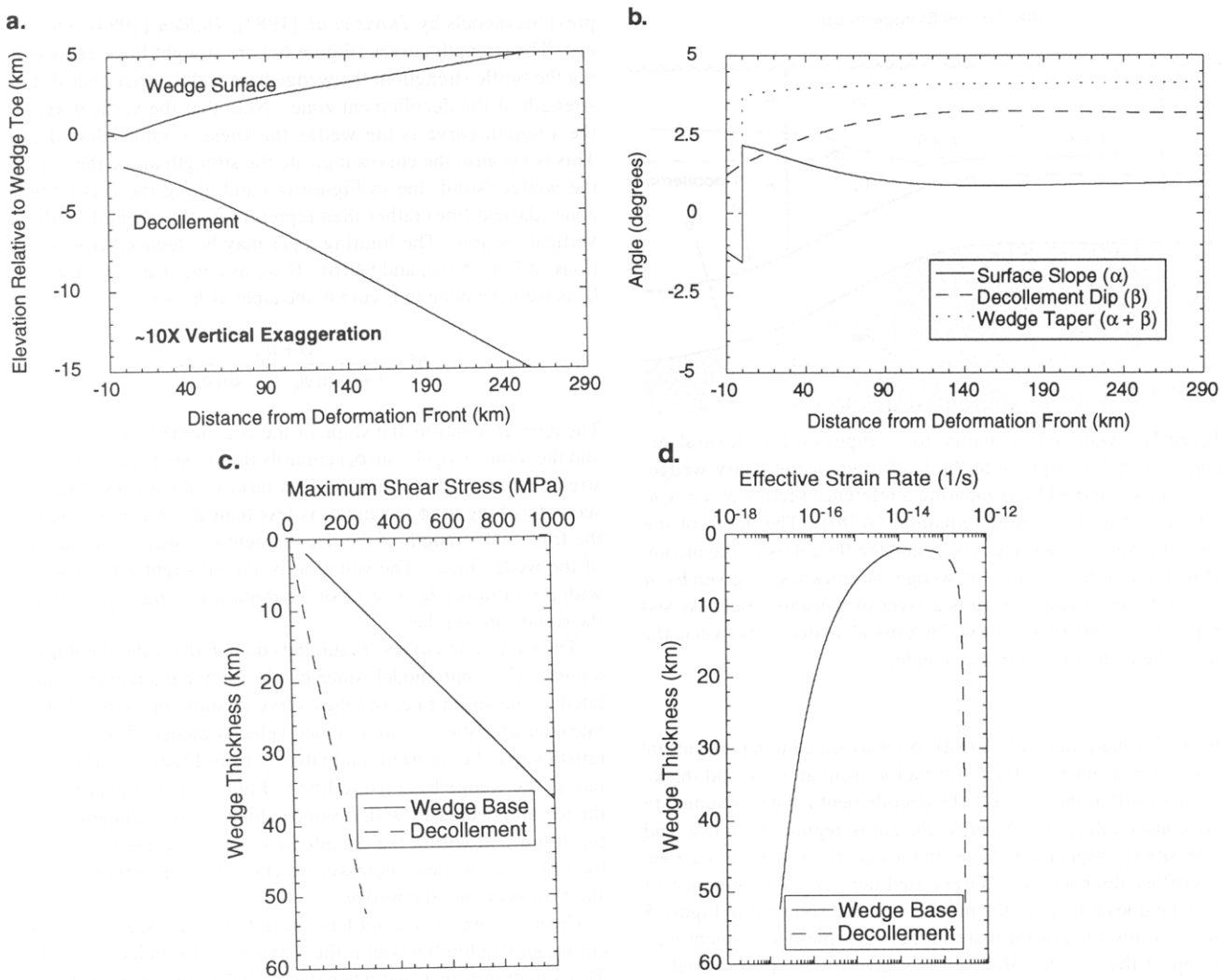

Figure 6. Predicted wedge characteristics for a purely brittle-frictional critical taper model. (a) The predicted wedge geometry, showing the positions of the decollement and the wedge surface. (b) The surface slope α, the decollement dip β, and the wedge taper, $\alpha + \beta$ as functions of distance from the wedge toe. Note how the wedge taper becomes nearly constant a short distance into the wedge. (c) The maximum shear stress along the wedge base and within the decollement zone as a function of wedge thickness. This plot does not represent the strength versus depth at some position within the wedge but instead represents the strength of the wedge base and the decollement as one moves from the toe of the wedge toward the interior. (d) The effective strain rate in the wedge base and within the decollement zone. Note that the strain rate within the wedge base is a maximum near the toe and decreases gradually toward the wedge interior, while the decollement strain rate is a minimum at the toe and increases rapidly to a nearly constant value.

gins to weaken, the wedge taper decreases, producing a flat wedge crest. There is a small "kink" in the strength and strain rate curves for the wedge base (Figures 7c and 7d), although this has no discernible effect on the predicted wedge geometry. This is a numerical artifact that may occur in regions of large curvature (x derivative of the wedge taper), or in regions where the wedge thickness is very small, as explained in Appendix A.

The situation described above and depicted in Figures 1 and 7 is not unique. It is also possible that the decollement could become ductile at a shallower depth than the wedge base. In this case, a steep slope region would not develop, and the wedge profile would consist of only two distinct regions: a gently dipping toe and a flat plateau. Alternatively, either the wedge base or the decollement (or both) could exhibit ductile behavior at the surface, yielding other types of wedge morphologies. Although these other scenarios are interesting and may be applicable to certain situations, we have chosen to concentrate on the type of morphology depicted in Figures 1 and 7, which we believe is representative of a number of terrestrial and Venusian fold-and-thrust belts. For this reason, we have selected examples (Uorsar Rupes, Maxwell Montes, and the Andes) where we believe the brittle-ductile transition plays an important role. Some terrestrial accretionary wedges (Taiwan, for example) can be completely described by a purely frictional wedge model. This may occur because the decollement never penetrates to a sufficient depth, or because lower frictional strengths or higher convergence velocities have pushed the brittle-ductile transitions to a much greater depth (see equations (A24), (A25), (A28), (A29), and Figure 7c).

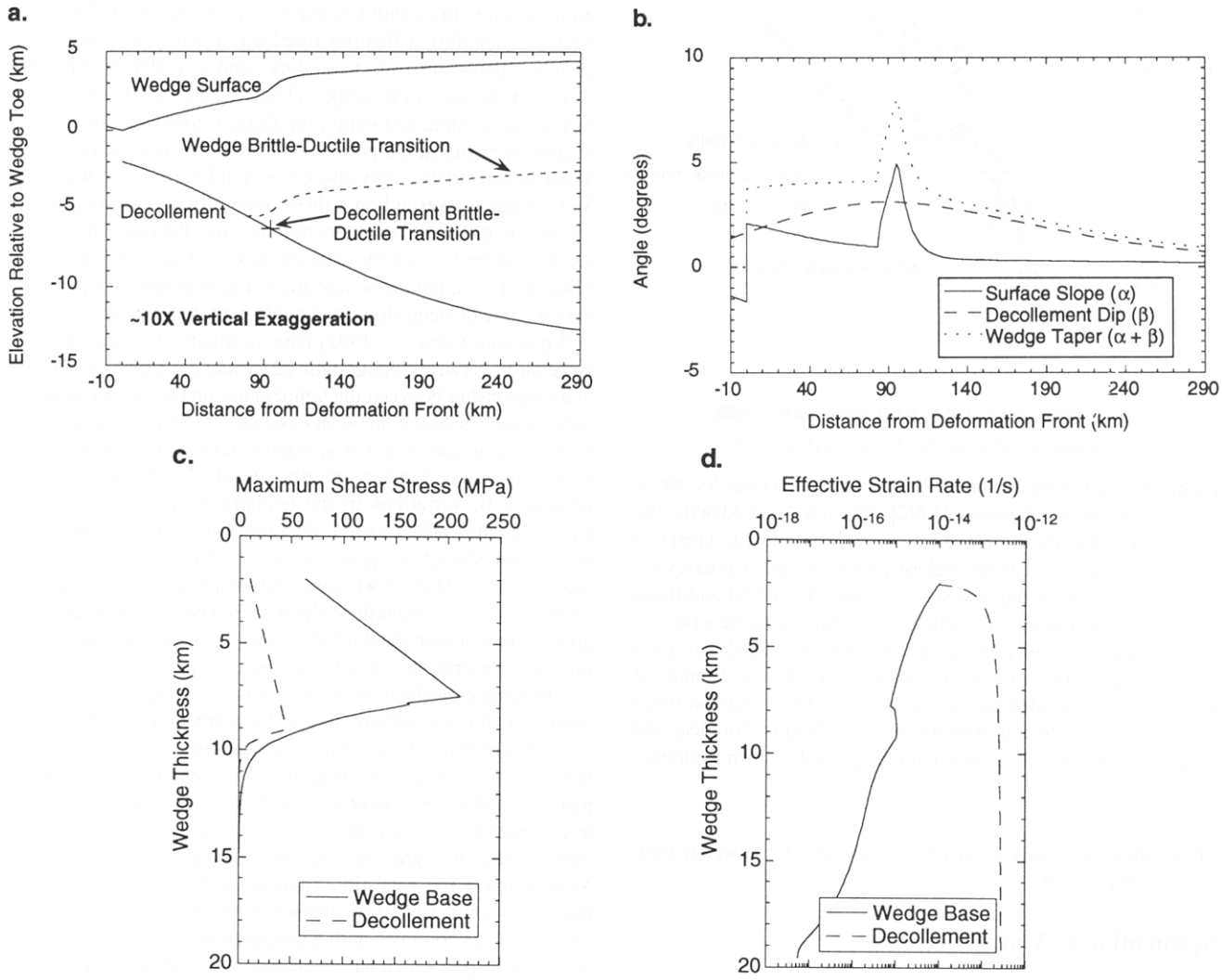

Figure 7. Same plots as Figure 6 for a brittle-ductile critical taper wedge. The geometry of this model (Figure 7a) shows the position of the brittle-ductile transition within the wedge and the position of the frictional-ductile transition along the decollement, as well as the wedge surface and decollement geometries. This model, unlike the purely frictional model, predicts a sharp increase in the wedge taper and surface slope at the point where the wedge brittle-ductile transition intersects the decollement, followed by a sharp decrease at the point where the decollement becomes ductile (Figure 7b). These points correspond to peaks in the strengths of the wedge base and the decollement zone, respectively (Figure 7c).

First-Order Wedge Characteristics

The observable features of a wedge (particularly on Venus) are the widths of the frictional and steeply sloping portions of the wedge (zones I and II in Figure 1a) and the maximum surface slopes of these two regions. The general wedge characteristics can be understood in terms of the brittle-ductile and frictional-ductile transitions within the wedge base and the decollement. The primary factors controlling wedge shape are the depths to the two transitions and the relative strengths of the wedge base and the decollement within the brittle portion of the wedge and at the decollement transition.

The width of the narrow-taper region (zone I in Figure 1a) corresponds to the distance of the wedge base transition from the wedge toe. In general, this distance will be closely related to the depth to the brittle-ductile transition within the wedge. The width of the steeply sloping region (zone II in Figure 1a) is equal to the horizontal distance between the wedge base transition and the decollement transition and is thus likely to be related to the difference in depths between the two transitions. The taper within the frictional portion of the wedge will vary slightly but will approach the limiting value given by equation (6). The closest approach to this limiting value will generally occur at the transition from brittle to ductile behavior within the wedge base, where the frictional portion of the wedge is thickest. This is true because the uniaxial compressive strength of the wedge material generally has some finite value, whereas the cohesive strength of the decollement is usually negligible. As the wedge becomes thicker, the increase in gravitational stress reduces the relative importance of the wedge cohesion, until the limiting case of a noncohesive wedge is attained (equation (6)). The maximum wedge taper is controlled by the relative magnitudes of the decollement strength at the brittle-ductile transition (the maximum decollement strength) and the wedge base strength at the same location: a large taper occurs if the strength of the decollement at its frictional-ductile transition (the dividing line between zones II and

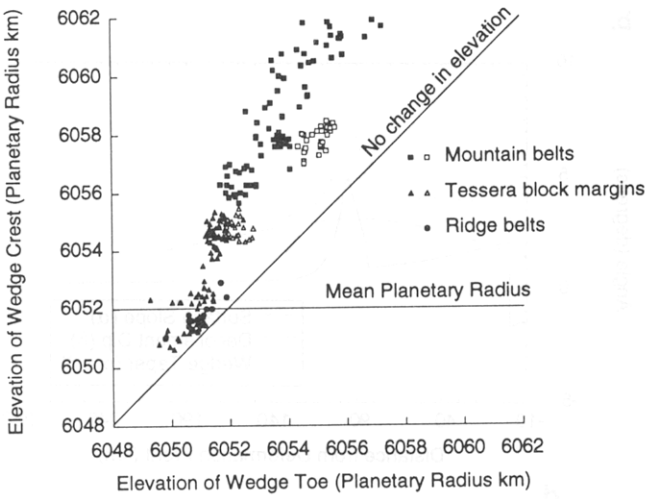

Figure 8. Plot of wedge crest elevation versus wedge toe elevation from *Suppe and Connors* [1992]. The relief of fold belts (the difference between the elevation of the toe and the crest) on Venus is a maximum at the highest elevations and decreases linearly to near zero at the lowest elevations. Most fold-and-thrust belts display a characteristic altimetric profile including a flexural foredeep and low-taper toe, a narrow zone of steep slopes and a relatively flat crest or plateau, as seen in Figures 2c and 2d. These belts are plotted as solid symbols. Other fold-and-thrust belts that do not display the characteristic flexural foredeep and have less relief than the linear trend are plotted as open symbols.

III in Figure 1a) is nearly equal to the strength of the wedge base at the same position.

Application to Venus

Observations

The Magellan mission has provided a wealth of information on the topography of Venus (in the form of radar altimetry) and on the structure of Venusian surface features from synthetic aperture radar (SAR) imagery. Among the many features that have been identified are several that exhibit surface structures characteristic of fold-and-thrust belts. Several such structures have been recognized by *Suppe and Connors* [1992], who have observed parallels between these features and terrestrial accretionary wedges. A viscous wedge theory has also been applied to the margin of Itzpopalotl tessera by *Vorder Bruegge and Fletcher* [1990].

Suppe and Connors [1992] have discovered that Venusian fold-and-thrust belts at higher elevations display a greater amount of relief than do wedges at lower elevations. We here define relief as the vertical distance between the wedge toe and the wedge crest. This correlation is seen in Figure 8, which is plot of wedge toe elevation versus wedge crest elevation. At the lowest elevations are the ridge belts, which typically have less than 1 km of relief. At somewhat higher elevations are the fold-and-thrust belts at the margins of tessera blocks, which generally display 4 km or less of relief. The mountain belts occur at the highest elevations, and these can have relief of 6 km or more.

Despite the differences in observed relief, the Venusian fold-and-thrust belts display certain structural similarities. Figure 9a, a radar image of the western margin of Maxwell Montes at about 64°N, 001°E, displays a moderately deformed toe region and an intensely deformed interior. Topographic profiles across this region (Figure 9b) exhibit features typical of many Venusian wedges, including a flexural foredeep, a gently sloping toe region, a narrow zone of steep slope, and a relatively flat crest. Note that the toe of the wedge, characterized by less intense deformation, is contained within the flexural foredeep. Intense deformation begins at the point where the slope increases abruptly. These characteristics may also be seen in Figure 9c, in which the SAR image is overlaid on a three-dimensional representation of the altimetry. Similar characteristics are displayed by Uorsar Rupes (Figure 10). In this case, the flexural foredeep is generally filled with lava, but the wedge still contains a narrow taper toe, a narrow zone of steep slope, and a relatively flat plateau.

Suppe and Connors [1992] have postulated that the observed correlation between topographic relief and elevation may be due to a relationship between the temperature on the decollement and the elevation at which the wedge occurs. If the temperature at the base of the wedge is lower at higher elevations, then we would expect to see a greater amount of relief. As discussed in Appendix B, variations in the temperature parameters should have a greater effect on the decollement strength than on the wedge base strength if $Q_d/n_d > Q_r/n$, which is true for our models (see Table 1). Thus, if we lower the temperature on the decollement, the ductile strength of the decollement will increase by a greater amount than the ductile strength of the wedge base, yielding a greater amount of relief (see Figure B3a).

One simple mechanism for obtaining this variation in the temperature is the atmospheric temperature gradient, which is about 8°C/km on Venus [*Kliore et al.*, 1985; *Lyons*, 1991]. The surface temperature of Venus is extremely high: about 470°C at mean planetary radius [*Kliore et al.*, 1985], so that rocks close to the brittle-ductile transition at mean planetary radius may be much more brittle at higher elevations. As an example, Maxwell Montes has a toe elevation approximately 5 km above mean planetary radius, so that the surface temperature at the toe is only ~430°C. This contrasts with a temperature of ~466°C at the toe of Uorsar Rupes, which has an elevation only about 0.5 km above mean planetary radius. Another mechanism for lowering the temperature on the decollement at higher elevations, also proposed by *Suppe and Connors* [1992], is that the planetary temperature gradient is isostatically coupled to the thickness of the lithosphere. Thus the planetary thermal gradient ∇T will be lower for regions of higher elevation. As mentioned previously, the thermal environment should also be related to the effective elastic thickness. Thus regions of lower surface temperature or thermal gradient should also have larger values for the effective elastic thickness, further increasing the amount of relief.

There has been some recent evidence that surface activity on Venus may have actually ceased as long as 500 m.y. ago, based on both morphological evidence and the observed correlation between gravity and topography [*Kerr*, 1993; *McNamee et al.*, 1993; *Solomon*, 1993; *Turcotte*, 1993; *Kerr*, 1994]. If this is true, then the compressive structures on Venus may actually be fossil features, representing a time average of the parameters that were appropriate at the time of their formation. The flexural parameters would represent lithospheric properties at the time the wedge was active. To first order, the resulting wedge morphology would depend primarily on the rates at which the convergence velocity (u_0) and the planetary thermal gradient (∇T) decreased with respect to each other. If the lithosphere cooled significantly while convergence was still occurring, the depth to the brittle-ductile transition would increase, pushing the steep slope and plateau regions farther back into the interior of the wedge. If, on the other hand, convergence ceased while the lithosphere was

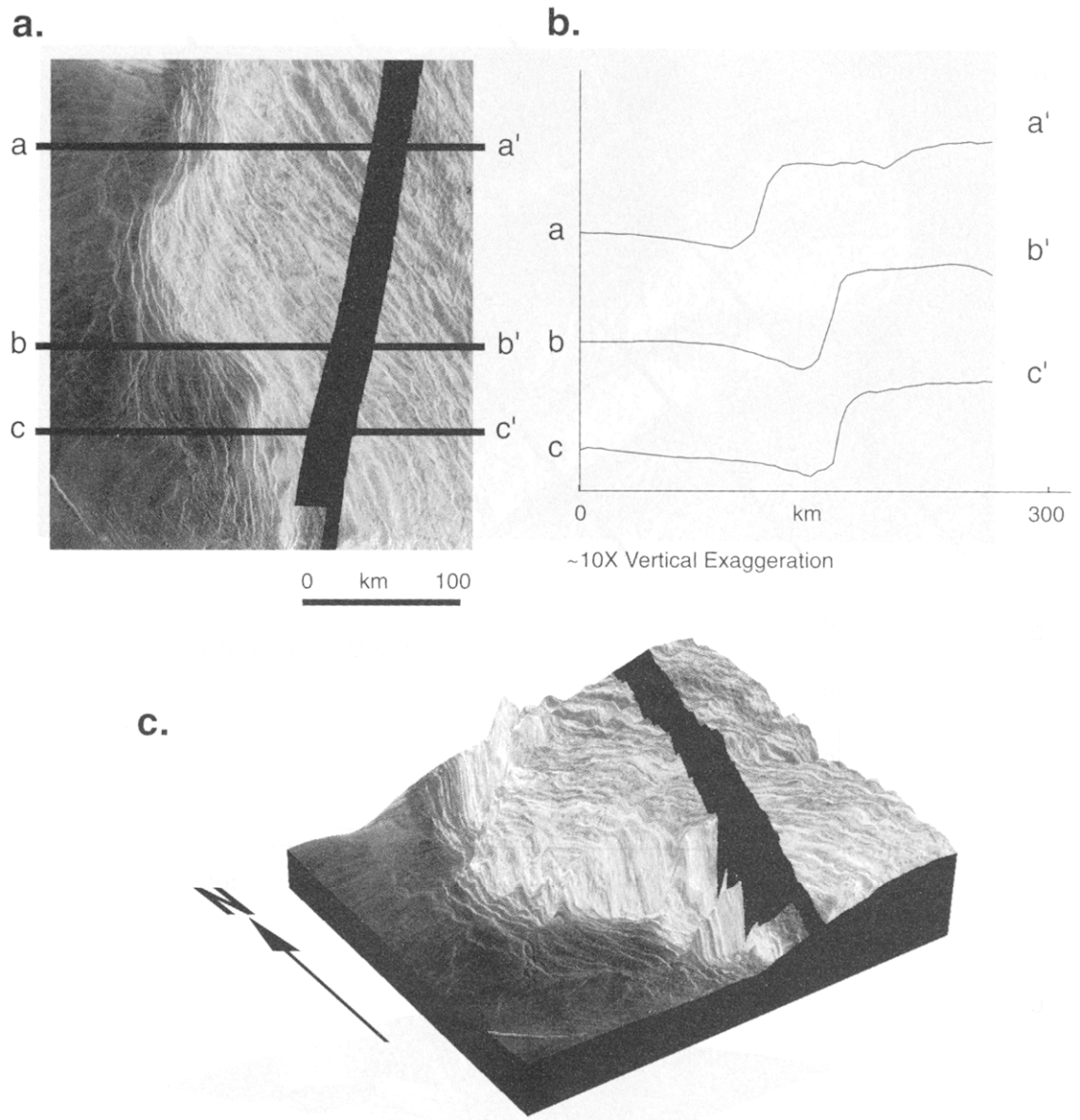

Figure 9. (a) SAR image of Maxwell Montes on Venus (b) with corresponding topographic profiles. These profiles are not quite perpendicular to strike, unlike the profile used in our modeling. (c) SAR data overlaid on altimetry data. This region displays the characteristic pattern consisting of a flexural foredeep and a gently sloping toe region (corresponding to the moderately deformed region at the left-hand side of the SAR image), a narrow, steeply sloping region, and a relatively flat plateau region.

still relatively hot, the depth to the brittle-ductile transition would decrease, moving the steep slope and plateau regions toward the toe of the wedge. We are not able to place constraints on the evolution of our model parameters over time, and it should be understood that the parameters used in our models may represent some sort of time-integrated average. Once a wedge has been produced, however, it is possible to maintain the same wedge shape, even when the driving forces have ceased, as long as the wedge is still in a stable configuration [*Dahlen*, 1984]. It is possible that this may presently be the case on Venus.

Parameter Values

To test our model, we computed predicted wedge shapes for profiles across Maxwell Montes and Uorsar Rupes. We were particularly interested to see if the observed correlation between topographic relief and elevation could be explained purely in terms of differences in temperature. To test this hypothesis, we selected a set of parameters for Maxwell Montes that produced a reasonable fit to the observed topography and that were relatively consistent with independent estimates of their values. We then used the same set of parameters to describe the shape of Uorsar Rupes, varying only the surface temperature T_0, the planetary temperature gradient ∇T, and the elastic thickness of the lithosphere H. The parameter values used are listed in Table 1. Note that the parameters are listed in the same groupings as used in Table B1a. Parameters that are not independently resolvable are lumped together.

As we stated before, there are large uncertainties in the parameters of our model, but data from the Magellan and Venera

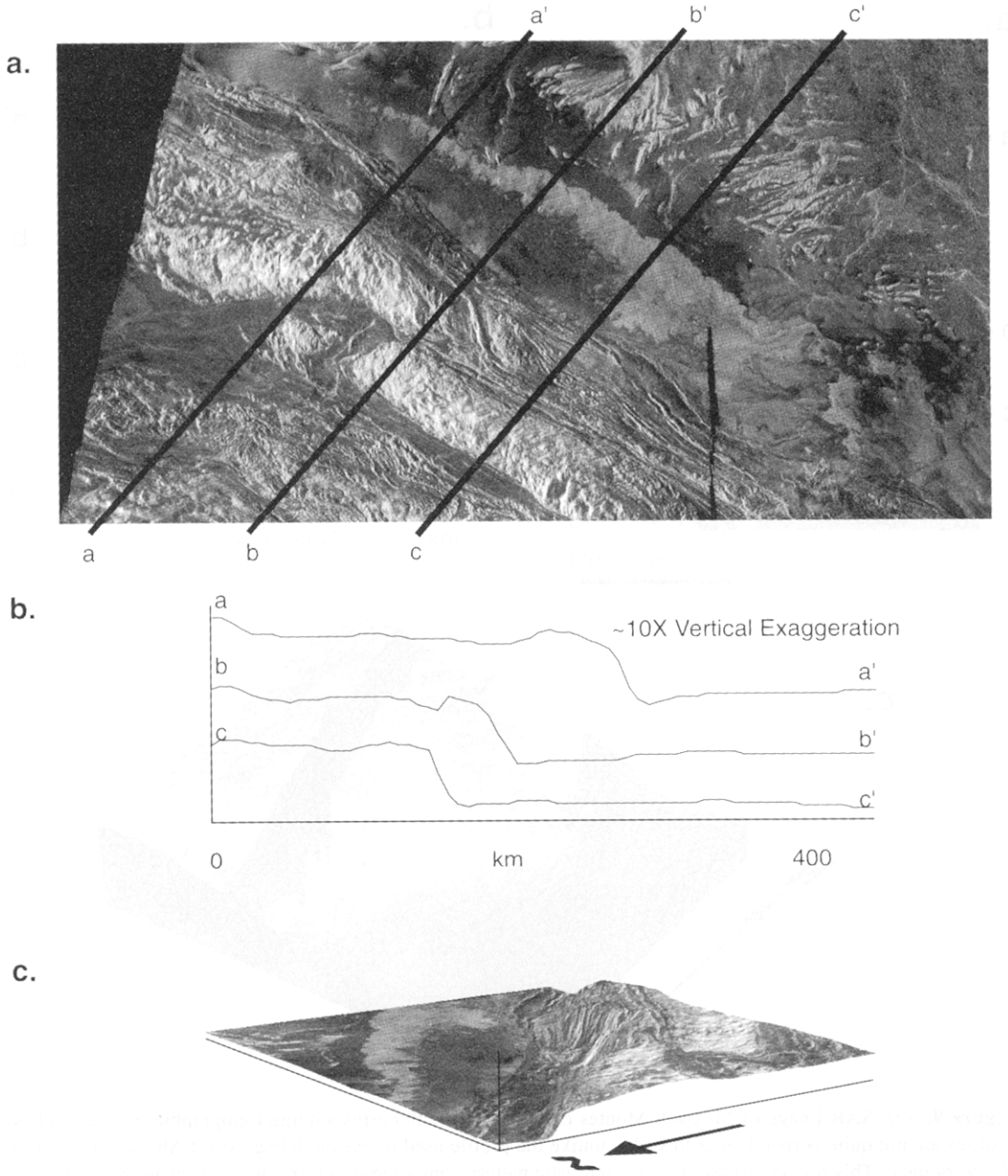

Figure 10. (a) SAR image of Uorsar Rupes on Venus (b) with corresponding topographic profiles. (c) SAR data overlaid on altimetry data. This region displays the same characteristic pattern of fold-and-thrust belts on Venus as does Maxwell Montes, although the amount of relief is less. In this case, the flexural foredeep is partially filled with lava.

missions allow us to place some constraints on our Venus models. The surface composition of Venus is thought to resemble that of diabase, based on data from the Venera landers, which indicated a tholeitic composition [*Surkov et al.*, 1983]. Furthermore, the low atmospheric density (~75 kg/m^3 [*Kliore et al.*, 1985]) relative to that of water indicates that $\lambda_d \approx \lambda_h \approx \rho_f \approx 0$ for our model. The absence of significant water vapor in the Venusian atmosphere [*Kaula*, 1990] implies that we should use rheological properties for "dry" rock samples. Although it is difficult to ascertain the thermal gradient within the planet, *Solomon and Head* [1990] have estimated gradients similar to those on Earth (15-25°C/km) based on analysis of lithospheric flexure in the Uorsar Rupes foredeep. There are several estimates of effective elastic thickness available for Venus. *Sandwell and Schubert* [1992] have obtained estimates of 15 to 40 km for the lithosphere beneath several Venusian topographic features.

We were able to assign several parameter values based on the information above, and on general knowledge of rock behavior. For the brittle-frictional rock properties, we assumed $\mu_d = \mu_h = 0.6$, $S_d = 0$, and $C_h = 88$ MPa. The values for the friction coefficients and the cohesion of the decollement are consistent with the results of *Byerlee* [1978], and the uniaxial compressive strength of the wedge base is consistent with an estimated cohesion of 25 MPa for crust composed of lava flows, sills, dikes, and faults and joints in nonoptimal orientations [*Suppe and Connors*, 1992].

There exists a fairly large volume of laboratory-derived flow

Table 1. Parameter Values Used for This Study

Parameter	Maxwell Montes	Uorsar Rupes	Andes
Decollement			
S_d, MPa	0.0	0.0	0.0
$\mu_d(1-\lambda_d)$, dimensionless	0.6	0.6	0.06
$(s_d)^{p_d}/\delta A_d$, MPa^{n_d} s / m	2.1×10^{-9}	2.1×10^{-9}	2.3×10^{-15}
Q_d, kJ/mol	290	290	250
n_d, dimensionless	1	1	1
Wedge base			
C_h, MPa	88	88	20
$\frac{(1-\lambda_h)\sin\phi_h}{1-\sin\phi_h}$, dimensionless	1.06	1.06	0.919
$\log_{10}A$, A in units of MPa^{-n} s^{-1}	-3.7	-3.7	-2.5
Q, kJ/mol	260	260	150
n, dimensionless	3.4	3.4	1.8
Decollement and wedge base			
h_0, km	0.5	0.5	2.0
u_0, cm/yr	2.0	2.0	1.0
ρ_c, kg/m^3	2700	2700	2600
ρ_w, kg/m^3	0	0	0
ρ_m, kg/m^3	3400	3400	3400
g, m/s^2	8.61	8.61	9.80
T_0, °C	430	466	20
∇T, °C/km	15	17	25
∇T_A, °C/km	8	8	8
Flexure			
H, km	30	30	25
E, GPa	100	100	100
ν, dimensionless	0.25	0.25	0.25

law parameters for rocks in the dislocation creep regime (see, for example, the compilation by *Kirby and Kronenberg* [1987]); however, difficulties arise when extrapolating these results to geological situations. There are large uncertainties in the parameters themselves, and it is also unlikely that the flow mechanisms observed in the laboratory can be extrapolated with complete confidence to geologic space-time scales (see *Strehlau and Meissner* [1987] for a description of the problems involved with extrapolating laboratory flow law results to geologic settings). Nevertheless, these results provide an important means for understanding the mechanical behavior of planetary lithospheres. We have therefore chosen to incorporate laboratory-derived flow laws into our model. To describe the ductile strength of the wedge base, we used the results of *Shelton and Tullis* [1981] for dislocation creep in dry diabase.

Quantitative studies of diffusion flow in rocks are not numerous at present. Most current results are for monomineralic samples, such as those of *Karato et al.* [1986] for synthetic olivine aggregates. Owing to the scarcity of parameter estimates for diffusion flow, we have simply chosen to use the results of *Karato et al.* [1986], using values for dry olivine in our Venus models and values for wet olivine in our Andes model. If future results for polyphase crustal rocks are significantly different from those for olivine, we will have to adjust our other model parameters accordingly. We selected a grain size s_d and decollement thickness δ that placed the ductile strength in the proper range of stresses. The preexponential factor that we used would be consistent with a grain size s_d of 0.127 μm and a decollement thickness δ of 100 m (or, alternatively, with values of $s_d = 0.402$ μm and $\delta = 1000$ m), assuming that the diffusion flow parameters are correct.

The average density of diabase is approximately 2900 kg/m^3 [*Turcotte and Schubert*, 1982]; however, to obtain the necessary relief for Maxwell Montes, we found that it was necessary to use a value of about 2700 kg/m^3. Maxwell Montes is located on the high plateau of Lakshmi Planum. It may be that this plateau is composed of a material slightly less dense than diabase (such as anorthosite). Since no landers have sampled the plateau thus far, the crustal density is relatively unconstrained. We assumed an average mantle density of 3400 kg/m^3. The convergence rate u_0 is virtually unconstrained, since we have no direct evidence of the rate at which movement is occurring on the surface of Venus. We assume that the rates are not significantly different from those on Earth and choose a convergence rate of 2 cm/yr. Likewise, the thickness of the incoming material at the deformation front h_0 is poorly constrained. *Suppe and Connors* [1992] have inferred a depth of approximately 1.5 km for the decollement near the toe of the Artemis Chasma fold belt; we assume a somewhat arbitrary value of 500 m for all of our Venusian models.

Results

Using the parameter values described above and assuming a surface temperature of 430°C at the toe of Maxwell Montes, a planetary temperature gradient of 15°C/km, and an elastic thickness of 30 km, we obtained the results of Figure 11a. Superimposed on the model results is an observed topographic profile across Maxwell Montes. Although the fit is not perfect, we seem to have predicted the principal features of the fold-and-thrust belt, consisting of a flexural forebulge and foredeep, a gently sloping toe, a steep rise, and a relatively flat plateau. The primary difference between our model and the observed topography is that we have underestimated the slope in the steep portion of the wedge. Magellan altimetry has a horizontal resolution of approximately 10 km at this latitude, so the exact slope of the steep region is poorly constrained. It is possible, however, that a different set of parameters could yield the observed steep slope. It is also possible that the discrepancy is due to inaccuracies in the small-angle approximation. We have found that at least for purely frictional wedges, the small-angle approximation consistently underestimates the surface slope when compared with the exact solution for a noncohesive wedge [*Dahlen*, 1984].

Our simplified velocity field also prevents the wedge from attaining an extremely high taper, due to the dependence of strain rate (and thus the ductile strength of the wedge base) on the wedge taper (see equations (A23), (A24), and (A25)). The wedge taper increases when the ductile strength of the wedge base decreases relative to the strength of the decollement; however, increasing the taper causes the strength of the wedge base to increase, pushing the taper back to a smaller value (see equation (A24)). The dependence of the wedge base strength on the wedge taper acts as a type of feedback mechanism, inhibiting the occurrence of extremely steep slopes. Despite these effects, the model provides a fairly good fit to the observed topography.

The complete geometry of our preferred model for Maxwell Montes is shown in Figure 12a, and the corresponding strength curve is shown in Figure 13a. The model predicts brittle behavior

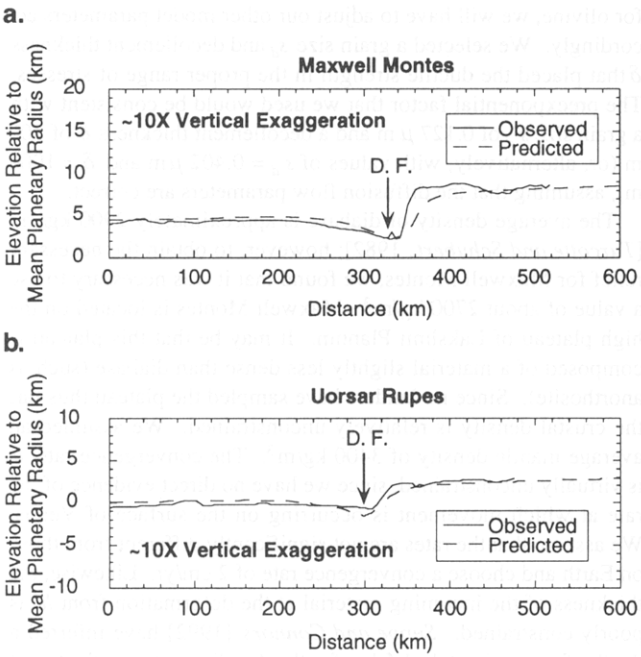

Figure 11. Observed and predicted surface elevations for (a) Maxwell Montes and (b) Uorsar Rupes. The deformation front (DF) is indicated with an arrow for each case. The only differences between the two models are the surface temperature (430°C for Maxwell Montes and 466°C for Uorsar Rupes) and the planetary thermal gradient (15°C/km for Maxwell Montes and 17°C/km for Uorsar Rupes). The principal difference between our model results and the observed topography is an underestimation of the slope in the steeply-sloping portion of the wedge. This is probably due to the small-angle approximation used in our solution, which tends to underestimate the wedge taper.

within the upper 2 or 3 km of the wedge (Figure 12a), and the decollement becomes ductile about 2 km below the point where the wedge brittle-ductile transition intersects the wedge base (Figure 13a). The strain rate within the decollement is fairly high, ranging from about 10^{-12} to 10^{-11} s^{-1}, whereas within the wedge the strain rate varies from about 10^{-13} s^{-1} at the toe to 10^{-18} s^{-1} near the back. To obtain the relatively steep surface slopes and high relief, it was necessary for the decollement strength to nearly equal the wedge base strength (Figure 13a). We accomplished this by varying the preexponential factor for the decollement ductile strength until an appropriate value was found.

We used the parameter values for our preferred Maxwell Montes model as the basis for our model of Uorsar Rupes. The elevation at the toe of Uorsar Rupes is about 0.5 km, yielding an estimated surface temperature of 466°C. We used the same elastic thickness as for Maxwell Montes, but increased the planetary thermal gradient to 17°C/km to obtain the results of Figure 11b. In this case we seem to have overestimated the depth of the foredeep; however, since the foredeep appears to be filled with lava, our predicted model is probably not too badly in error. The model geometry is shown in Figure 12b, and the corresponding strength curves are shown in Figure 13b. An interesting feature of this model is that due to our assumed velocity field, the brittle-ductile transition within the wedge intersects the surface at some distance back from the wedge toe. If we were to interpret this literally, we would expect the surface in the wedge interior to display a different style of deformation (i.e., nonbrittle); however, owing to the uncertainties in our assumed velocity field and in the other model parameters, we are reluctant to attach any special significance to the predicted ductile behavior at the surface of the wedge. The predicted strength curves (Figure 13b) are significantly different from those of our Maxwell Montes model, particularly for the decollement. The decollement strength relative to the wedge base strength is significantly less for our Uorsar Rupes model than for the Maxwell Montes model, and the vertical distance between the two brittle-ductile transitions is less than 1 km. These factors result in a wedge with a relatively small taper overall and with a fairly narrow zone of steep slope.

A comparison of Figures 11a and 11b indicates that it is entirely possible that the observed correlation between the relief of Venusian fold-and-thrust belts and the elevation at which they occur may be due simply to differences in the thermal environment. In our models, it was only necessary to change the surface temperature by 36°C and the planetary thermal gradient by 2°C/km to produce the observed difference in relief. The geometry of Venusian wedges is particularly sensitive to changes in the thermal environment, due to the high surface temperature. Since the brittle-ductile transitions are typically less than 5 km from the surface (see Figures 13a and 13b), small changes in the thermal environment can have a large effect on the predicted wedge geometry. Terrestrial fold-and-thrust belts, as typified by the Andean example in the next section, are much less sensitive to small changes in surface temperature.

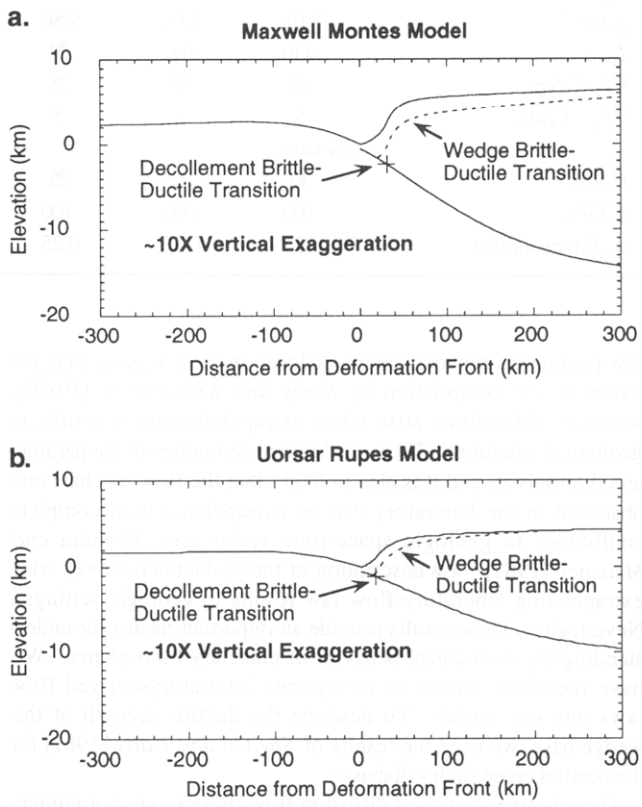

Figure 12. Predicted geometry of our models for (a) Maxwell Montes and (b) Uorsar Rupes. The brittle-ductile transition within the wedge (dashed line) remains below the surface for the Maxwell Montes model but intersects the surface for the Uorsar Rupes model. The frictional-ductile transition on the decollement (shown with a cross) occurs at a greater depth for the Maxwell Montes model, resulting in a greater amount of topographic re lief.

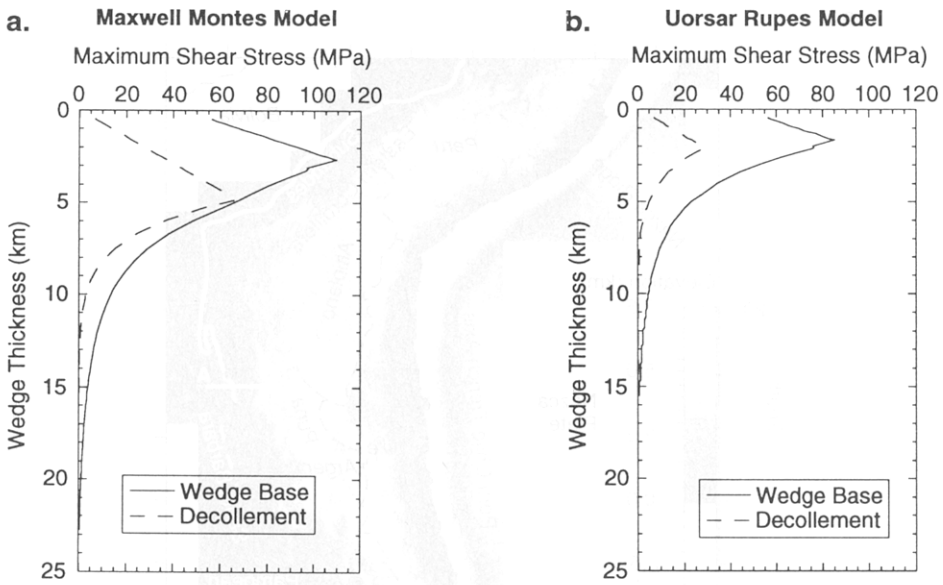

Figure 13. Predicted strengths of the wedge base and the decollement for our models of (a) Maxwell Montes and (b) Uorsar Rupes. For the Maxwell Montes model, the decollement strength at the point where it becomes ductile is nearly equal to the strength of the wedge base, and the vertical separation between the two transitions is nearly 3 km, yielding a wedge with a large amount of topographic relief. The Uorsar Rupes model predicts that the two Coulomb-ductile transitions occur at nearly the same depth, and the decollement strength is always significantly less than the strength of the wedge base. The result is a wedge with moderate relief.

Application to the Andes

Observations

The Andean belt (Figure 14a) is a continuous feature along the western margin of South America, although the character changes along strike. Below about 27°S, the eastern margin of the Andes is characterized by the thick-skinned tectonic style of the Pampean Ranges [*Allmendinger et al.*, 1983]. Between 27° and 24°S lies the structurally complex Santa Barbara transitional system. North of 24°S, the structural geometry is typified by the thin-skinned style shown in geologic cross section by *Mingramm et al.* [1979] (Figure 14b). In this region, the eastern margin of the Andes displays the classic characteristics of a thin-skinned fold-and-thrust belt and thus seems a likely candidate for the application of critical taper wedge mechanics.

The eastern Andean margin of this region is commonly classified into different regions on the basis of tectonic style, which we believe correspond to zones I, II, and III of our critical taper model. These regions have been described very well by *Allmendinger et al.* [1983]. Farthest to the east lies the Subandean belt, a narrow fold-and-thrust belt along the eastern margin of the Andes which is characterized by relatively gentle topography. The predominant deformational style appears to be brittle-frictional failure, which would correspond to zone I of our model. Westward of the Subandean belt lies the Eastern Cordillera, a narrow zone characterized by complex systems of thrust and reverse faults. The Eastern Cordillera displays much steeper surface slopes than do the Subandes, and we believe that this corresponds to zone II of our model. Still farther to the west lies the Altiplano, which is also known as the Puna in Argentina. This is a high, mountainous plateau region which we believe represents zone III of the critical taper model.

Although the eastern Andean margin is structurally complex, it appears to be amenable to treatment by a two-dimensional critical taper wedge model. There is considerable volcanism in the Altiplano; however, extrusive material appears to compose a relatively small volume of the plateau [*Isacks*, 1988], and it thus appears likely that the topography of the region can be explained in terms of crustal shortening and thickening. In fact, the hypothesized cross section of the Andes near 20.5°S by *Isacks* [1988] (Figure 15) looks remarkably like our brittle-ductile model. There are obviously some complexities not accounted for by the model, but the large-scale features seem to be adequately explained. We have made use of the digital topographic data set of *Isacks* [1988] in our modeling of the eastern Andean margin. A gray scale representation of this data set is shown in Figure 14a. We chose to model the region at 20.80°S, although our model could equally well fit several profiles between 20° and 22°S.

Parameter Values

The parameters used in our Andes model are listed in Table 1. The frictional properties of the model were constrained, for the most part, by the extremely small slope of the Subandean fold-and-thrust belt. We varied the frictional properties of the wedge base and decollement until we obtained a reasonably small slope. It is not possible to independently resolve the two parameters λ_h and ϕ_h, or the parameters μ_d and λ_d (see equations (1) and (2)). We used values of $\mu_d(1 - \lambda_d) = 0.06$, and $(1 - \lambda_h) \sin \phi_h/(1 - \sin \phi_h) = 0.92$. These values would be consistent, for example, with values of $\phi_h = 40°$, $\mu_d = 0.6$, $\lambda_h = 0.5$, and $\lambda_d = 0.9$. The frictional strength of the decollement seems fairly low, but this was necessary to match the small observed slopes. The uniaxial compressive strength of the wedge base was chosen to be 20 MPa (a reasonable value for sedimentary rocks), and the cohesion of the decollement was assumed to be zero [*Byerlee*, 1978].

We used the rheological properties of wet quartzite (listed in a compilation by *Strehlau and Meissner* [1987]) to describe dislocation creep in the wedge base. The ductile strength of the

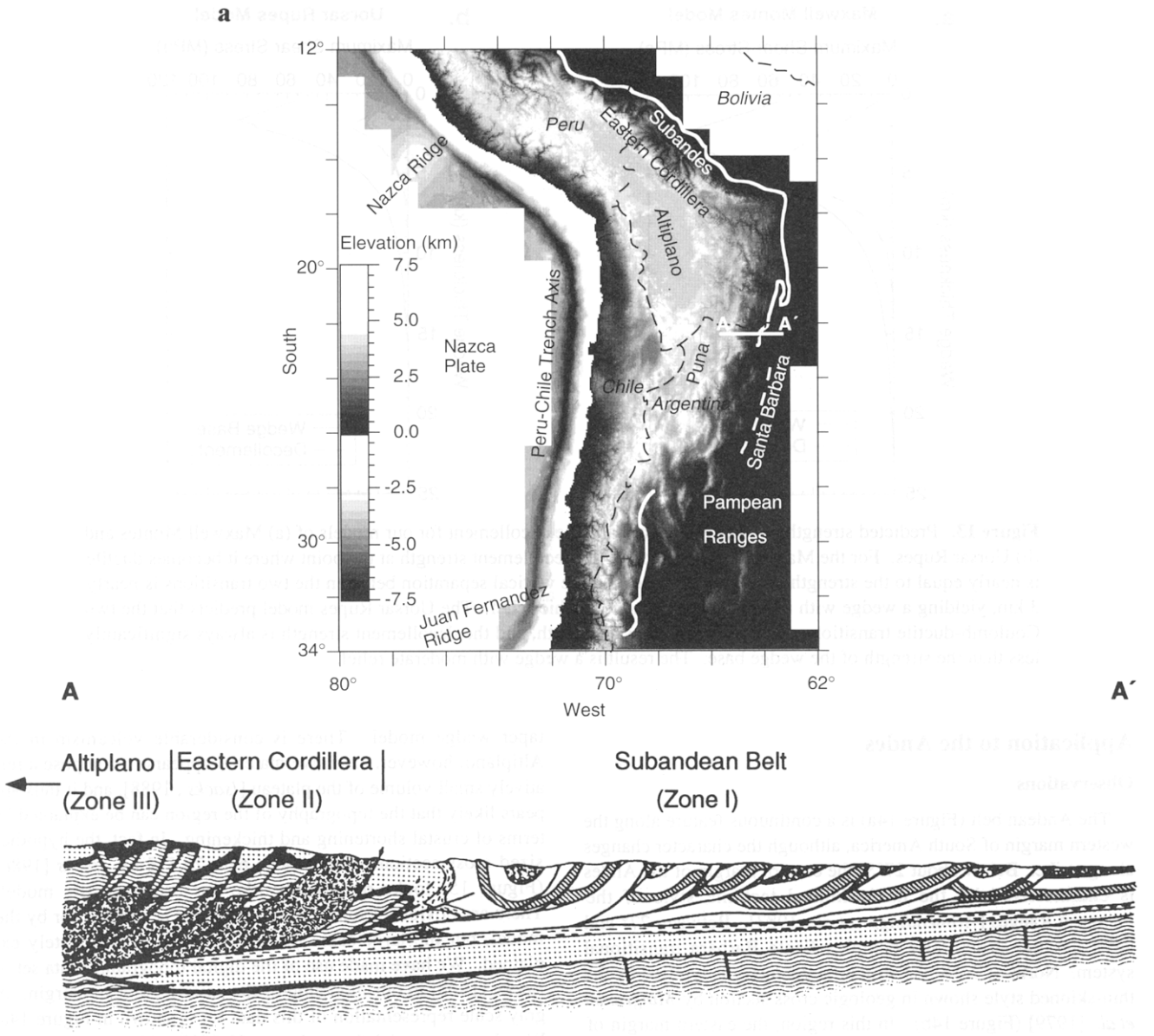

Figure 14. (a) The coastline, country borders, and certain geographic and tectonic provinces in western South America overlaid on a gray scale representation of digital topography, both from *Isacks* [1988]. (b) A geologic cross section constructed by *Mingramm et al.* [1979], located approximately at line AA' on the map (22.5°S). This cross section seems to typify the structure of the eastern margin of the Andes between about 24°S and 18°S, which is characterized by a thin-skinned fold-and-thrust style of deformation. We believe that the different tectonic regions in this area correspond to the three regions of our model. The Subandean belt corresponds to the narrow taper frictional toe of our model (zone I), the Eastern Cordillera corresponds to the steeply sloping region of our model (zone II), and the Altiplano corresponds to the flat plateau of our model (zone III).

decollement was assumed to be controlled by diffusion flow in wet olivine [*Karato et al.*, 1986], and the grain size s_d and decollement thickness δ were again selected to place the ductile strength curve in the proper range of stresses. As described previously, our assumed values for the rheological properties of the decollement are restricted by the availability of data. At present, we are forced to use rheological properties for olivine, although this is obviously not a reasonable rheology for a decollement within continental crust. This may explain the relatively small grain size we were required to use to obtain reasonable results (s_d = 0.015 μm for a decollement thickness δ of 1000 m).

The eastern Andes are composed of a wide variety of sedimentary and crystalline rocks, which could have a large range of densities; we selected an average crustal density of 2600 kg/m^3 and a mantle density of 3400 kg/m^3. *Molnar and Lyon-Caen* [1988] depict a scenario for the eastern Andes with a few millimeters per year of convergence. As a rough estimate, we assume a convergence rate u_0 of 1 cm/yr. We estimate that the minimum thickness of the incoming material is about 2 km, our assumed value for h_0. The thickness of the elastic lithosphere in the Andes near this region has been estimated to be between 20 and 55 km by *Lyon-Caen et al.* [1985] and to be about 25 km by *Salvador and*

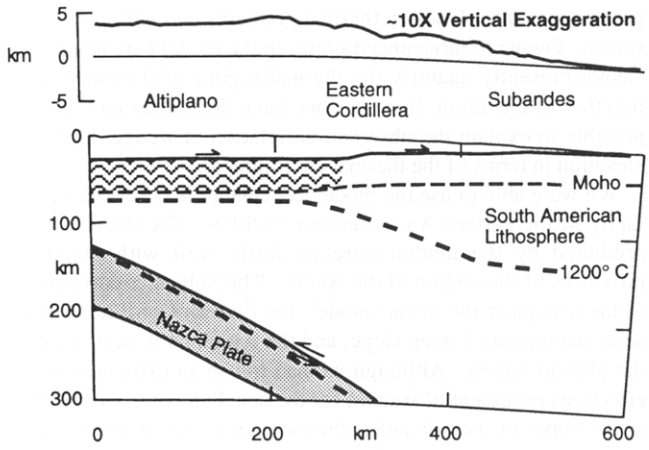

Figure 15. Hypothesized structure of the Andes near 20.5°S from *Isacks* [1988]. We have only shown the structure from the Altiplano eastward. The wavy lines indicate a region of shortened and thickened ductile lower crust, and a hypothesized 1200°C isotherm is shown with a thick dashed line. Note that this interpretation indicates overthrusting of the upper crust onto the foreland along a relatively continuous fault, which is consistent with our critical taper model.

Kellogg [1991]. We selected a value of 25 km. We estimate the surface temperature at the wedge toe to be about 20°C, and we chose a thermal gradient (∇T) of 25°C/km. We selected an atmospheric temperature gradient ∇T_A of 8°C/km, based on a dry adiabatic lapse rate of 10°C/km and a moist adiabatic lapse rate of 6°C/km [*Moran and Morgan* , 1991].

Results

Using the parameters described above, we produced the predicted profile shown in Figure 16a. Although the actual topography of the Andes is considerably more irregular, the model is able to match the observed topography fairly well. A primary difference between the Andes model and those for Venusian wedges is that the brittle-frictional toe of the wedge is significantly wider in the Andes. This is due both to the lower surface temperature and to the extremely low frictional strength of the decollement. The features of the model may be seen more clearly in Figure 16b. The model displays a very narrow taper, cohesive toe, corresponding to the Subandes, a steep rise, corresponding to the Eastern Cordillera, and the flat plateau of the Altiplano. The decollement dip is very shallow, generally less than 2°. This may be somewhat low when compared with the profile of Figure 14b; however, the decollement dip could be increased with the proper

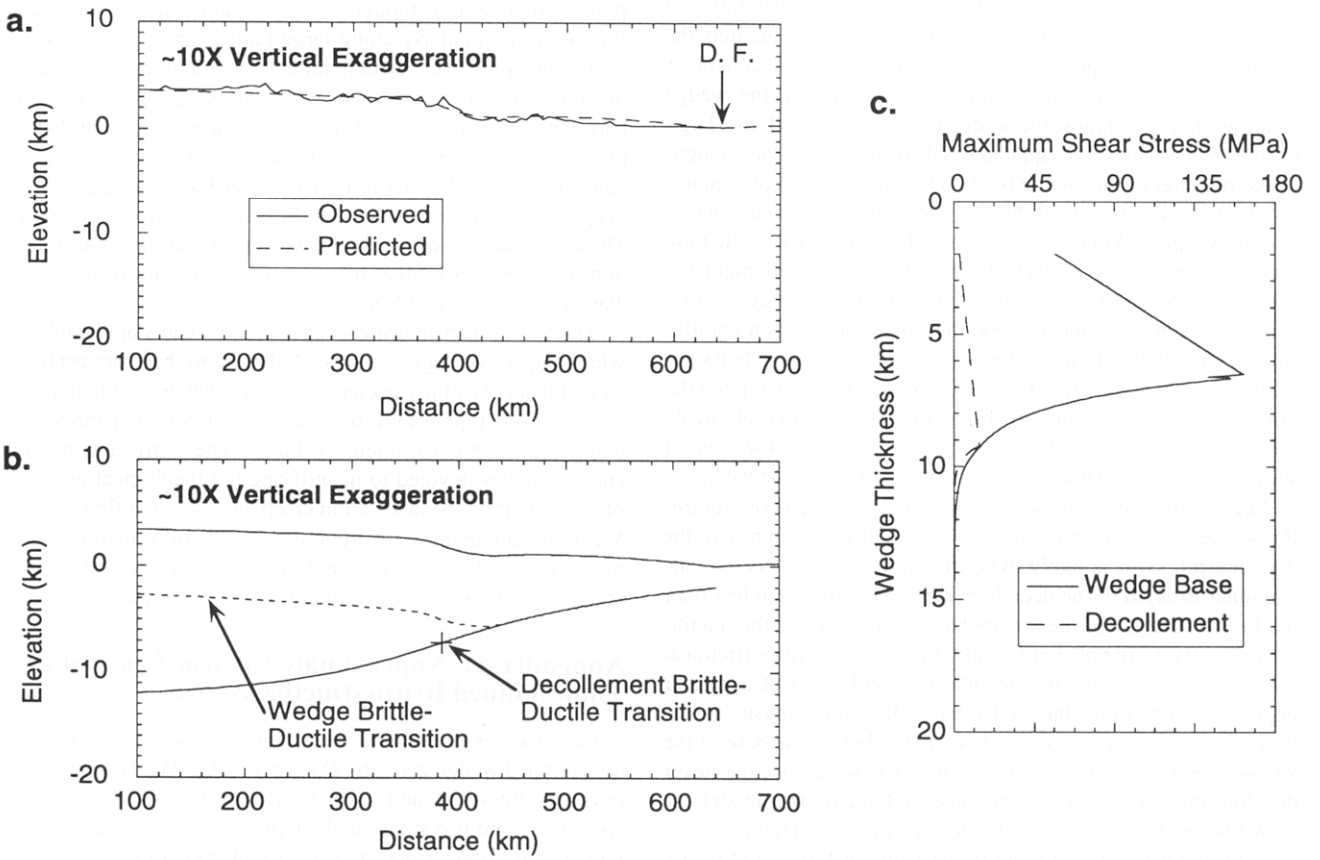

Figure 16. Results of our critical taper model of the eastern Andes near 20.80°S. (a) Predicted and observed surface elevations. The model provides a good fit to the observed topography, although the steep slopes of the Eastern Cordillera are slightly underestimated, probably as a result of our small-angle approximation. (b) Predicted geometry for our Andes model. This model has a very long, narrow taper toe when compared with the Venusian models (Figure 16), due to both the smaller strength of the decollement and the greater depth of the brittle-ductile transition within the wedge (dashed line). (c) The strength of the wedge base and the decollement zone as a function of wedge thickness. Note that the wedge base is significantly stronger than the decollement zone, except at the point where the decollement becomes ductile.

selection of parameters. The thickness of the frictional portion of the wedge is significantly greater than for the Venus models, as expected, and there is a greater distance between the two brittle-ductile transitions. The reason for the greater amount of separation is clear from the stress profiles of Figure 16c. The frictional strength curve for the decollement appears to be a near-vertical line when contrasted with the frictional strength of the wedge base. The frictional-ductile transition for the decollement is thus pushed downward with respect to the wedge base brittle-ductile transition. The low value of basal shear stress at the brittle-ductile transition is also responsible for the relatively modest increase in surface slope of the Eastern Cordillera. The predicted strain rates computed for this model are fairly typical of terrestrial values. In the decollement, values range from about 10^{-14} to 10^{-13} s^{-1}, while the strain rate in the wedge varies from 10^{-17} to 10^{-14} s^{-1}.

Conclusions

We have presented a generalized model that predicts the equilibrium shape for an accretionary wedge/fold-and-thrust belt with brittle-frictional and/or ductile deformation. The equilibrium shape is determined by the brittle-frictional and ductile properties of the wedge material and the decollement; the thermal environment; the elastic thickness of the lithosphere; the convergence rate; the densities of the wedge material, mantle, and overlying fluid (or dense gas); the thickness of the incoming material; and the thickness of the decollement zone. The model predicts the geometry of the wedge surface as well as that of the decollement zone. Although the actual expressions describing the wedge shape are fairly complex, the wedge taper is controlled, to a large extent, by the ratio of the applied basal shear stress to the strength of the material in the wedge base. This simple concept explains the dramatic changes in slope that are observed in many accretionary wedges. When the wedge base becomes ductile, the ratio increases, producing a larger taper; when the decollement becomes ductile, the ratio decreases, resulting in a wedge with a narrower taper. For most cases, the model predicts an equilibrium shape that characterizes most fold-and-thrust belts on Venus, as well as several on Earth (although we have applied the model only to the Andes in this study). This "stereotypical" shape consists of a small-taper, Coulomb toe, a narrow zone of steep slope, and a relatively flat plateau at the top of the wedge.

The occurrence of the wedge shape described above requires the wedge base to become ductile at a shallower depth than the decollement. This is likely to be true in most cases, because the frictional strength of the decollement is generally much less than the brittle strength of the wedge base. Therefore, if the ductile strength curves are not significantly different, the brittle-frictional and ductile curves for the decollement will cross at a greater depth than they do for the wedge base. In certain unusual situations, the decollement may become ductile before the base of the wedge (see Figures B2 and B3). In this case, the wedge never develops the steep surface slopes observed in our other models.

We were able to apply the model, with a large degree of success, to two different fold-and-thrust belts on Venus and to the eastern side of the Andes at about 21°S. For the Venusian wedges, we were able to explain the observed variations in topography purely on the basis of differences in the thermal environment. Wedges at higher elevations, which exhibit much greater relief, may be explained as a result of lower surface temperature (or possibly a lower planetary thermal gradient) and a larger elastic thickness of the lithosphere. The lower-relief wedges observed at lower elevations are explained by higher surface temperatures and/or planetary thermal gradients and a thinner lithosphere. Owing to large uncertainties in the model parameters, we cannot presently quantify the thermal regime of the planet as a function of elevation; however, we have demonstrated that it is possible to explain the observed correlation of wedge relief and elevation in terms of the thermal environment.

We were able to use the model to explain the observed topography of the eastern Andes around 20.80°S. The three regions predicted by the model correlate fairly well with the three provinces of this region of the Andes. The Subandes correspond to the low-taper toe of our model, the Eastern Cordillera represents the region of steep slope, and the Altiplano is equivalent to the plateau region. Although we had to use an extremely small effective coefficient of friction for the decollement to explain the small slopes of the Subandes, the parameters we used were generally consistent with what is presently known about the Andes.

The model can also correctly predict the observed differences between terrestrial and Venusian accretionary wedges, based on first-order differences in the planetary environments. Two of the principal differences between Earth and Venus are the absence of significant amounts of water vapor on Venus and the relatively high surface temperature. The relatively low atmospheric density of Venus relative to that of water, combined with the absence of significant amounts of water vapor, indicates that the effects of pore fluid pressure are likely to be relatively small. On Earth, pore fluid pressure is thought to play a significant role in rock deformation, particularly along large fault zones. Thus terrestrial accretionary wedges, which should have significantly weaker decollement zones than their Venusian counterparts, will have narrower cohesive toes that require a greater horizontal distance to achieve the same decollement depth. At the same time, the depth to the brittle-ductile transition on Earth should be much deeper than on Venus, due to the lower surface temperature. These two factors, coupled together, mean that the cohesive portions of terrestrial wedges have a much greater horizontal extent than do those found on Venus.

The brittle-ductile critical taper model seems applicable to a wide range of geologic settings. Although we have not performed a careful survey of parameter space, we have been able to predict the observed topography of a number of fold-and-thrust belts using reasonable parameter values. There are a number of current studies devoted to quantifying the rheological properties of rocks, both in the dislocation creep and diffusion flow regimes. We anticipate that the incorporation of this information into our model will provide a better representation of accretionary wedges and should allow us to constrain the other model parameters.

Appendix A: Approximate Critical Taper of a Thin-Skinned Brittle-Ductile Wedge

Our analysis is based on the approximate general theory for a thin-skinned wedge given by *Dahlen* [1990]. We assume that the principal stresses σ_1 and σ_3 are nearly horizontal and vertical, respectively, and use small-angle approximations for all terms involving the surface slope α or the decollement dip β. The resulting theory is quasi-analytical. The analysis allows for the possibility of hydrostatic or nonhydrostatic pore fluid within the wedge and water or a dense atmosphere above the wedge, as shown in Figures 3a and 3b. The primary difference between the present model and that of *Dahlen* [1990] is that we explicitly include the effects of temperature-dependent power law rheology. The prominent features of the model can be traced to the transition from brittle-frictional to ductile behavior within the wedge

and on the decollement. We first derive a general critical taper equation for a thin-skinned wedge and then define specific terms describing brittle-frictional and ductile behavior. These terms are included in the general equation, yielding a critical taper equation for a brittle-ductile accretionary wedge. Finally, we discuss the incorporation of flexural isostasy into the model.

General Critical Taper Equation

We initially assume x and z axes that are locally aligned with the top of the wedge (Figure 3a). The small-angle equations of static equilibrium within the wedge are then

$$\frac{\partial \sigma_{xx}}{\partial x}+\frac{\partial \sigma_{xz}}{\partial z}-\rho_c g\alpha \approx 0, \tag{A1a}$$

$$\frac{\partial \sigma_{xz}}{\partial x}+\frac{\partial \sigma_{zz}}{\partial z}+\rho_c g \approx 0, \tag{A1b}$$

where ρ_c is the constant density of the wedge material. Our convention in (A1) and elsewhere is that compressive stresses are negative. The quantity $\partial\sigma_{xz}/\partial x$ can be ignored to first order in equation (A1b) [*Dahlen*, 1990]. Integration then yields the following result for the vertical stress due to the overlying water and porous wedge material:

$$\sigma_{zz} \approx \sigma_3 \approx -\rho_f g d-\rho_c g z, \tag{A2}$$

where d and ρ_f are the depth and density of the overlying water, respectively.

Now suppose that the differential stress, $\Delta = \sigma_3 - \sigma_1$, is a specified function of x and z. In the small-angle approximation, the horizontal stress is

$$\sigma_{xx} \approx \sigma_1 \approx -\rho_f g d-\rho_c g z-\Delta. \tag{A3}$$

The shear traction on the basal decollement fault, in the small angle approximation, is

$$\tau_d \approx (\sigma_3-\sigma_1)(\alpha+\beta)+\sigma_{xz}. \tag{A4}$$

The shear stress, σ_{xz}, is obtained from equation (A1a):

$$\frac{\partial \sigma_{xz}}{\partial z} \approx \rho_c g\alpha-\frac{\partial \sigma_{xx}}{\partial x} \approx (\rho_c-\rho_f) g\alpha+\frac{\partial \Delta}{\partial x}. \tag{A5}$$

We have used the fact that $d' \approx -\alpha$, where the prime denotes differentiation with respect to x. We then integrate to obtain σ_{xz} on the wedge base, $z = h$:

$$\sigma_{xz} \approx (\rho_c-\rho_f) gh\alpha+\int_0^h \frac{\partial \Delta}{\partial x}\,dz. \tag{A6}$$

Substituting this relationship into (A4), the shear traction on the basal decollement is

$$\tau_d \approx (\rho_c-\rho_f) gh\alpha+\Delta_h(\alpha+\beta)+\int_0^h \frac{\partial \Delta}{\partial x}\,dz, \tag{A7}$$

where $\Delta_h = \Delta(h)$. Solving this for the taper, $h' \approx \alpha + \beta$, we obtain the general critical taper equation:

$$\alpha+\beta \approx h' \approx \frac{(\rho_c-\rho_f) gh\beta+\tau_d-\int_0^h \frac{\partial \Delta}{\partial x}\,dz}{(\rho_c-\rho_f) gh+\Delta_h}. \tag{A8}$$

Having obtained this result, it is then permissible to ignore the slight variable tilt of the x and z axes at different points in the wedge, as shown in Figure 3b [*Dahlen*, 1990]. Equation (A8) represents an approximate differential equation that can be integrated to find the wedge thickness $h(x)$, given the appropriate boundary condition(s) at the toe of the wedge. Ignoring the last term in the numerator, we observe that the taper is controlled primarily by the ratio of the basal shear traction to the strength of the material in the wedge base. In the limit, as the basal shear traction and wedge base strength approach zero, the taper is equal to the decollement dip β and the surface slope α is equal to zero.

Equations for a Brittle-Frictional Wedge

For the brittle-frictional case, we assume that the differential stress within the wedge is controlled by a brittle Mohr-Coulomb yield criterion:

$$\Delta^{\text{brit}} = 2\left[S\cos\phi+(p-p_f)\sin\phi\right], \tag{A9}$$

where S is the cohesion, ϕ is the angle of internal friction, and p_f is the pore fluid pressure. The pressure p is given by

$$p = -\frac{1}{2}(\sigma_{xx}+\sigma_{zz}). \tag{A10}$$

A more useful form of (A9) is obtained by substituting the following relationship for the pore fluid pressure:

$$p_f = \rho_f g d+\lambda\rho_c g z, \tag{A11}$$

where

$$\lambda = \frac{p_f-\rho_f g d}{-\sigma_{zz}-\rho_f g d} \tag{A12}$$

is the generalized *Hubbert and Rubey* [1959] pore fluid to lithostatic pressure ratio. The brittle strength within the wedge is then

$$\Delta^{\text{brit}} \approx C+2\rho_c g z(1-\lambda)\left(\frac{\sin\phi}{1-\sin\phi}\right), \tag{A13}$$

where C is the uniaxial compressive strength [*Jaeger and Cook*, 1979, p. 80, pp. 96 - 97]:

$$C = 2S\left(\frac{\cos\phi}{1-\sin\phi}\right). \tag{A14}$$

To simplify our analysis, we assume that C, ϕ, and λ are constant throughout the wedge. We adopt a simple frictional law for the basal shear traction [e.g., *Byerlee*, 1978]:

$$\tau_d^{\text{fric}} = S_d+\mu_d(1-\lambda_d)\rho_c g h, \tag{A15}$$

where the subscript d denotes parameter values within the decollement zone. From (A8), the critical taper equation for a

purely frictional wedge is thus

$$\alpha+\beta \approx h' \approx \frac{(\rho_c-\rho_f)gh\beta+\tau_d^{\text{fric}}}{(\rho_c-\rho_f)gh+\Delta_h^{\text{brit}}}, \tag{A16}$$

where Δ_h^{brit} and τ_d^{fric} are defined by equations (A13) (at $z = h$) and (A15), respectively.

Equations for a Ductile Wedge

In the ductile portion of the wedge, we assume that the differential stress is controlled by a thermally activated power law relationship [e.g., *Karato et al.*, 1986],

$$\Delta^{\text{duct}} = \left(\frac{\dot{\varepsilon}s^p}{A}\right)^{\frac{1}{n}} \exp\left(\frac{Q}{nRT}\right), \tag{A17}$$

where $\dot{\varepsilon}$ is the effective strain rate, A is the generalized viscosity coefficient, n is the stress power law exponent, Q is the activation energy, s is the grain size, p is the grain size exponent, R is the ideal gas constant, and T is the absolute temperature. Within the wedge, we assume that viscous flow is dominated by dislocation creep, so that $n > 1$ and $p \approx 0$ [*Karato et al.*, 1986]. In the decollement zone, we assume that the grain size is sufficiently small that diffusion creep is the dominant deformational mechanism [*Rutter and Brodie*, 1988; *Tullis and Yund*, 1991]. For this case, $n \approx 1$ and $p > 1$ [*Karato et al.*, 1986].

We may include the effects of a linear temperature gradient within the planet ∇T and a linear atmospheric temperature gradient ∇T_A by introducing the following two variables:

$$k = \frac{\nabla T}{T_0}, \tag{A18a}$$

$$k_A = \frac{\nabla T_A}{T_0}, \tag{A18b}$$

where T_0 is the absolute surface temperature at the toe of the wedge (the beginning of the deformation front in Figures 3a and 3b). The ductile flow law, (A17), then becomes

$$\Delta^{\text{duct}} = \left(\frac{\dot{\varepsilon}s^p}{A}\right)^{\frac{1}{n}} \exp\left[\frac{Q}{nRT_0(1+kz-k_Ae+k_Ae_0)}\right], \tag{A19}$$

where e is the wedge elevation and e_0 is the elevation at the wedge toe.

At this point, the simplest procedure would be to assume a constant strain rate. This is unlikely to be true in a deforming wedge, however, and we adopt a somewhat more realistic deformation field (Figure 4); we assume that the horizontal velocity is independent of depth and that mass is conserved. If the velocity of the incoming material is u_0 and flow is incompressible, the wedge velocity field is

$$u_x \approx \frac{u_0h_0}{h}, \tag{A20a}$$

$$u_z \approx \frac{u_0h_0zh'}{h^2}, \tag{A20b}$$

where h_0 is the thickness of the incoming material at the wedge toe ($x = 0$ in Figure 4).

We would now like to find the effective strain rate,

$$\dot{\varepsilon} = \sqrt{\frac{1}{2}\left(\dot{\varepsilon}_{xx}^2+\dot{\varepsilon}_{zz}^2\right)+\dot{\varepsilon}_{xz}^2}. \tag{A21}$$

Within the wedge, the strain-rate components are

$$\dot{\varepsilon}_{xx} = \frac{\partial u_x}{\partial x} \approx \frac{-u_0h_0h'}{h^2}, \tag{A22a}$$

$$\dot{\varepsilon}_{zz} = \frac{\partial u_z}{\partial z} \approx \frac{u_0h_0h'}{h^2}, \tag{A22b}$$

$$\dot{\varepsilon}_{xz} = \frac{1}{2}\left(\frac{\partial u_x}{\partial z}+\frac{\partial u_z}{\partial x}\right) \approx \frac{u_0h_0z}{h^2}\left(\frac{h''}{2}-\frac{h'^2}{h}\right). \tag{A22c}$$

It is easy to see that the second term of equation (A22c) is of second order when compared to equations (A22a) and (A22b). It is less obvious that the first term of this equation is also of second order; however, we have found that the shear strain rate (equation (A22c)) accounts for no more than 5% of the effective strain rate. Thus, for our purposes, $\dot{\varepsilon}_{xz} \approx 0$, and the effective strain rate within the wedge is

$$\dot{\varepsilon} \approx \frac{u_0h_0|h'|}{h^2}. \tag{A23}$$

The differential stress within the wedge is then

$$\Delta^{\text{duct}} \approx \left(\frac{F_0|h'|}{h^2}\right)^{\frac{1}{n}} \exp\left(\frac{F_1}{F_2+kz-k_Ae}\right), \tag{A24}$$

where

$$F_0 = \frac{u_0h_0s^p}{A}, \tag{A25a}$$

$$F_1 = \frac{Q}{nRT_0}, \tag{A25b}$$

$$F_2 = 1+k_Ae_0. \tag{A25c}$$

We must now specify the shear traction along the basal decollement τ_d^{duct}. We assume a decollement zone of constant finite thickness δ (Figure 4). Within this zone, the differential stress is controlled by power law flow (equation (A19)). At the bottom of the decollement zone, the velocity is equal to the velocity of the incoming material, u_0. To first order, the velocity difference (slip rate) between the bottom and top of the decollement zone is, from (A20),

$$\Delta u_d \approx u_0\left(1-\frac{h_0}{h}\right). \tag{A26}$$

The effective strain rate within the decollement zone is thus

$$\dot{\varepsilon}_d \approx \frac{u_0}{\delta}\left|1-\frac{h_0}{h}\right|, \tag{A27}$$

and the basal shear traction is

$$\tau_d^{duct} \approx \frac{1}{2}\left(G_0 \left| 1 - \frac{h_0}{h} \right| \right)^{\frac{1}{n_d}} \exp\left(\frac{G_1}{F_2 + kh - k_A e} \right), \quad \text{(A28)}$$

where

$$G_0 = \frac{u_0 (s_d)^{p_d}}{\delta A_d}, \quad \text{(A29a)}$$

$$G_1 = \frac{Q_d}{n_d R T_0}, \quad \text{(A29b)}$$

and the subscript d denotes parameter values within the decollement zone.

Equations (A24) and (A28) may now be substituted into (A8) to find the critical taper equation for a ductile wedge:

$$h' \approx \frac{(\rho_c - \rho_f) g h \beta + \tau_d^{\text{duct}}(h,e) - L\left(h, z_w^{\text{trans}}, e, h', e', h''\right)}{(\rho_c - \rho_f) g h + \Delta_h^{\text{duct}}(h,e,h')}, \quad \text{(A30)}$$

where

$$\begin{aligned} L = \frac{1}{kn}\left(\frac{F_0 |h'|}{h^2} \right)^{\frac{1}{n}} \Bigg\{ & \left(\frac{h''}{h'} - \frac{2h'}{h} \right) \\ & \Bigg[F_1 \,\mathrm{Ei}\left(\frac{F_1}{F_2 + kz_w^{\text{trans}} - k_A e} \right) - F_1 \,\mathrm{Ei}\left(\frac{F_1}{F_2 + kh - k_A e} \right) \\ & - (k_A e - kh - F_2) \exp\left(\frac{F_1}{F_2 + kh - k_A e} \right) \\ & + (k_A e - kz_w^{\text{trans}} - F_2) \exp\left(\frac{F_1}{F_2 + kz_w^{\text{trans}} - k_A e} \right) \Bigg] \\ & + k_A n e' \Bigg[\exp\left(\frac{F_1}{F_2 + kz_w^{\text{trans}} - k_A e} \right) \\ & - \exp\left(\frac{F_1}{F_2 + kh - k_A e} \right) \Bigg] \Bigg\}, \end{aligned} \quad \text{(A31)}$$

and

$$\begin{aligned} \mathrm{Ei}(x) &= \int_{-\infty}^{x} \frac{\exp(t)}{t} dt \qquad [x < 0], \\ \mathrm{Ei}(x) &= -\lim_{\varepsilon \to +0} \left(\int_{-x}^{-\varepsilon} \frac{\exp(-t)}{t} dt + \int_{\varepsilon}^{\infty} \frac{\exp(-t)}{t} dt \right) \qquad [x > 0] \end{aligned} \quad \text{(A32)}$$

is the exponential integral [*Gradshteyn and Ryzhik*, 1980]. The term L appears since the differential stress in the ductile regime depends on $h(x)$ and $h'(x)$ (equation (A24)), so that $L = \partial\Delta/\partial x$ is nonzero below the wedge brittle-ductile transition, $z = z_w^{\text{trans}}$.

Ordinarily, the ductile portion of the wedge base strength curve has a negative slope ($\partial\Delta_h^{\text{duct}}/\partial x < 0$); however, it may have a positive slope when $h''/h' > 2h'/h$ (see equation (A31)), a situation that may arise in regions of large curvature and/or small wedge thickness. This results in a "kink" in the ductile portion of the wedge base strength curve in some cases (see Figure 7c) corresponding to a kink in the strain rate curve (Figure 7d).

Brittle-Ductile Critical Taper Equation

For a critically-tapered wedge incorporating both brittle-frictional and ductile behavior, we rewrite (A8) as

$$\alpha + \beta \approx h' \approx \frac{(\rho_c - \rho_f) g h \beta + \tau_d - J}{(\rho_c - \rho_f) g h + \Delta_h}. \quad \text{(A33)}$$

The value of τ_d depends on whether the decollement is behaving in a brittle or ductile manner, and the values of Δ_h and J are dependent on the mode of deformation in the wedge basal material overlying the decollement zone. The dominant mode for each case will be that which predicts the smallest differential stress for a particular set of parameters; this may be determined by evaluating the following two functions:

$$F_d = 2\left(\tau_d^{\text{fric}} - \tau_d^{\text{duct}} \right) \quad \text{(A34)}$$

for the decollement, and

$$F_h = \Delta_h^{\text{brit}} - \Delta_h^{\text{duct}} \quad \text{(A35)}$$

for the wedge base. The value of h for which $F_d = 0$ defines the transition from frictional to ductile behavior within the decollement. If $F_d < 0$, the decollement behaves frictionally, while if $F_d > 0$, the decollement is in the ductile regime. In a similar manner, the wedge base is in the brittle regime for $F_h < 0$ and in the ductile regime for $F_h > 0$. The vertical position of the decollement frictional-ductile transition $z = z_d^{\text{trans}}$ is defined as the value of z for which $F_d = 0$. Similarly, the vertical position of the wedge brittle-ductile transition $z = z_w^{\text{trans}}$ is defined by $F_h = 0$. The wedge base brittle-ductile transition z_h^{trans}, described at the beginning of this paper, is the specific value of z_w^{trans} where the wedge brittle-ductile transition intersects the decollement.

The combination of positive and negative values for F_d and F_h lead to four possible sets of values for τ_d, Δ_h, and J. For $F_d < 0$, $\tau_d = \tau_d^{\text{fric}}$, while for $F_d > 0$, $\tau_d = \tau_d^{\text{duct}}$. For $F_h < 0$, $\Delta_h = \Delta_h^{\text{brit}}$ and $J = 0$, while for $F_h > 0$, $\Delta_h = \Delta_h^{\text{duct}}$ and $J = L$. Equation (A33) is integrated numerically, using the appropriate values for these parameters at each point. Typically, the toe of the wedge is completely frictional (F_h, $F_d < 0$), so that it is only necessary to specify the thickness at the wedge toe, h_0. When equation (A33) becomes second order ($F_h > 0$), the last known values of h and h' are used to begin the integration. If equation (A33) is second order at the toe of the wedge, an approximate initial taper is computed using (A33) without the term J. We assign a minimum value for the decollement strain rate at $x = 0$, since $\dot{\varepsilon}_d = 0$ for $h = h_0$ (see equation (A27)); otherwise, the basal shear traction would be zero at the wedge toe (equation (A28)).

Incorporation of Flexural Isostasy

As a first step toward allowing for flexural isostasy in the model, we consider the case of complete local isostasy. The geometry of the wedge is shown in Figure 5. The depth of the water (or dense atmosphere) above the wedge is d and its density is ρ_f. The density of the wedge material is ρ_c. The wedge thickness is $h(x) = e(x) + w(x)$, where $e(x)$ is the elevation of the surface of the wedge and $w(x)$ is the depth to the decollement. Both of these distances are measured from a reference elevation e_r, far from the wedge toe at position x_r (Figure 5). The depth of water at x_r is d_r, and the wedge is assumed to have constant thickness h_0 between

$x = x_r$ and $x = 0$ (the beginning of the deformation front). Below depth $z = h$, there is a layer of constant thickness and unspecified density, and beneath this layer is mantle material of density ρ_m.

Noting that $d(x) = d_r - e(x)$, we can isostatically balance our reference column at $x = x_r$ against a column through an arbitrary position in the wedge:

$$w(\rho_m - \rho_f) = h(\rho_c - \rho_f) + h_0(\rho_m - \rho_c). \quad \text{(A36)}$$

Taking the derivative with respect to x, and observing that $w' \approx \beta$, we obtain

$$\beta \approx \frac{h'(\rho_c - \rho_f)}{(\rho_m - \rho_f)}. \quad \text{(A37)}$$

This equation may be substituted into (A33) to obtain the solution for a locally isostatic accretionary wedge.

Turning now to the flexural problem, we must first determine the loads acting upon the elastic plate. The total load may be deduced from equation (A36) and written in terms of $e(x)$ and $w(x)$:

$$q(x) = eg(\rho_c - \rho_f) - g(w - h_0)(\rho_m - \rho_c), \quad \text{(A38)}$$

where positive loads are downward. The first term of (A38) is the topographic load, and the second term is the restoring force.

Treating the decollement surface (or its imaginary continuation to the left of the deformation front) as the top of an elastic plate, the equation for flexure of the plate in the absence of horizontal loads is [*Turcotte and Schubert*, 1982]

$$D\frac{d^4w}{dx^4} = q(x), \quad \text{(A39)}$$

where w is the vertical deflection of the plate and

$$D = \frac{EH^3}{12(1 - \nu^2)} \quad \text{(A40)}$$

is its flexural rigidity. The thickness of the plate is H, and E and ν are its Young's modulus and Poisson's ratio, respectively. For our problem, the equation may be written

$$D\frac{d^4w}{dx^4} + g(w - h_0)(\rho_m - \rho_c) = eg(\rho_c - \rho_f). \quad \text{(A41)}$$

Taking the derivative with respect to x, we obtain

$$D\frac{d^4\beta}{dx^4} + \beta g(\rho_m - \rho_c) = \alpha g(\rho_c - \rho_f). \quad \text{(A42)}$$

Turcotte and Schubert [1982] give the solution for an elastic plate subjected to a vertical line load. This may be viewed as a Green's function solution to the following problem:

$$D\frac{d^4G}{dx^4} + Gg(\rho_m - \rho_c) = \delta(x). \quad \text{(A43)}$$

The solution is

$$G(x) = \frac{a^3}{8D}\exp\left(-\left|\frac{x}{a}\right|\right)\left(\cos\left|\frac{x}{a}\right| + \sin\left|\frac{x}{a}\right|\right), \quad \text{(A44)}$$

where

$$a = \left[\frac{4D}{(\rho_m - \rho_c)g}\right]^{\frac{1}{4}}. \quad \text{(A45)}$$

Applying this solution to our problem, the decollement dip may be written as a function of the surface slope:

$$\beta(x) = \frac{(\rho_c - \rho_f)}{2a(\rho_m - \rho_c)}\int_{-\infty}^{\infty}\alpha(x')\exp\left(-\left|\frac{x - x'}{a}\right|\right)\left(\cos\left|\frac{x - x'}{a}\right| + \sin\left|\frac{x - x'}{a}\right|\right)dx'. \quad \text{(A46)}$$

The problem is solved iteratively, using the locally isostatic solution (equations (A33) and (A37)) as a starting point. The surface slopes computed from this solution are then used in (A46) to find new values for the decollement dip. The difference between the new and old values is computed, and a fraction of this difference is added to the old values to yield current estimates of $\beta(x)$ (using the computed new values as the current estimates proved to be unstable). These estimates are then used in (A33), and the process is continued until the average difference between new and old values is acceptably small. We were usually able to obtain convergence in 30 to 60 iterations, requiring 15 to 30 min of computation time on a Sun Sparcstation 2.

Although we believe that our model provides a realistic representation of the macroscale characteristics of fold-and-thrust belts, there are several limitations. Since the model is steady state, we cannot trace the evolution of a fold-and-thrust belt. Instead, we determine its equilibrium state and are thus unable to account for dynamical aspects, such as underplating and uplift. Since we do not actually solve the equations of motion in our model, we must also assume a velocity field. This is probably not a serious limitation; however, we have not yet performed a quantitative comparison between our velocity field and that of other models. A final limitation is the one-sided nature of our model. Many fold-and-thrust belts are actually two-sided (convergence is occurring from both directions). This may have some influence on our model, but the effect is probably only significant deep in the interior of the wedge. Despite these limitations, we believe that our model offers a reasonable description of the geometry of fold-and-thrust belts over sufficiently long length and time scales.

Appendix B: Effects of Model Parameters on Observable Wedge Characteristics

As discussed in the model characteristics section, the first-order effect of each model parameter on the predicted wedge shape can be understood in terms of how it affects (1) the depth (z_h^{trans}) at which the wedge base first becomes ductile, (2) the depth (z_d^{trans}) at which the decollement becomes ductile, (3) the strength [$\Delta_h(z_h^{\text{trans}})$] of the wedge base at its brittle-ductile transition, (4) the strength [$\tau_d(z_h^{\text{trans}})$] of the decollement at the wedge base transition, (5) the strength [$\tau_d(z_d^{\text{trans}})$] of the decollement at its frictional-ductile transition, and (6) the strength [$\Delta_h(z_d^{\text{trans}})$] of the wedge base at the decollement transition. These effects may be evaluated by examining equations (A13), (A15), (A24), (A28), (A34), and (A35). Table B1a lists the predicted effects of positive changes in the model parameters on these six quantities, and the resulting influence on the width of the narrow taper region, the width of the steeply sloping region, the brittle-frictional taper, and the maximum wedge taper. The variables used in this table are described in Table B1b.

Table B1a. Predicted Effects of Parameters on Wedge Characteristics

Parameter	z_h^{trans}	z_d^{trans}	$\Delta_h(z_h^{trans})$	$\tau_d(z_h^{trans})$	$\Delta_h(z_d^{trans})$	$\tau_d(z_d^{trans})$	Zone I Width	Zone II Width	Coulomb Taper	Maximum Taper
				Decollement						
S_d		–*		+		+		–	+	+
$\mu_d(1-\lambda_d)$		–?		+		+		–	+	+
$(s_d)^{p_d}/\delta A_d$		+				+		+		+
Q_d		+				+		+		+
				Wedge base						
C_h	–		+				–*	+	–	
$\frac{(1-\lambda_h)\sin\phi_h}{1-\sin\phi_h}$	–		+				–*	+	–	
A	–		–		–		–	+	+?	+
Q	+		+		+		+	–	–	–
				Decollement and wedge base						
h_0	+	–	+		+	–	+*	–	–?	–
u_0	+	++?	+		+	++	+	+*	–	+*
ρ_c	–	--?	+	++		+	–	–	+	+
T_0	–	--	–		–*	--	–	–	+*	–
∇T	–	--	–		–*	--	–	–	+*	–
∇T_A	+	++	+		+*	++	+	+	–?	+*

Anticipated effects of an increase in parameter values on the depth from the wedge surface to the brittle-ductile transition within the wedge base, z_h^{trans}, the depth to the decollement frictional-ductile transition, z_d^{trans}, the strength of the wedge base at z_h^{trans}, $\Delta_h(z_h^{trans})$, the strength of the decollement at z_h^{trans}, $\tau_d(z_h^{trans})$, the strength of the wedge base at z_d^{trans}, $\Delta_h(z_d^{trans})$, and the strength of the decollement at z_d^{trans}, $\tau_d(z_d^{trans})$. The probable effects on the widths of zones I and II, the brittle-frictional (Coulomb) taper, and the maximum taper are also shown. These results are based on a simple analysis of the parameter effects on the frictional and viscous strengths of the wedge base and the decollement zone. Test cases were used to determine whether the predicted effects could be verified. The symbols used are as follows: blank space, no direct effect; dash, quantity is decreased; plus, quantity is increased; double dash, quantity is decreased by a relatively large amount; double plus, quantity is increased by a relatively large amount; asterisk, observed trend is opposite of predicted trend; and question mark, predicted trend not verified.

Table B1b. Descriptions of Variables Used in Table B1a

Variable	Description
S_d	decollement cohesion
μ_d	decollement friction coefficient
λ_d	decollement pore fluid pressure ratio
s_d	decollement grain size
p_d	decollement grain size exponent
δ	decollement thickness
A_d	decollement viscosity coefficient
Q_d	generalized decollement activation energy
C_h	wedge base uniaxial compressive strength
ϕ_h	wedge base angle of internal friction
λ_h	wedge base pore fluid pressure ratio
A	generalized wedge viscosity coefficient
Q	wedge activation energy
h_0	thickness of incoming material
u_0	relative convergence velocity
ρ_c	average wedge density
T_0	surface temperature at wedge toe
∇T	planetary thermal gradient
∇T_A	atmospheric thermal gradient

Table B1a is subdivided into three regions: parameters that directly affect only the decollement characteristics, those that have a direct influence only on the wedge base characteristics, and parameters that affect both the decollement and the wedge base. None of the parameters can truly affect the strength of the decollement or the wedge base independently of the other; the strengths are coupled because of the dependence of Δ_h^{duct} on wedge taper h' (see equation (A24)). Only in the case of a purely Coulomb wedge are the strengths of the decollement and wedge base independent of each other. Table B1a is a guide to the expected effects of the various model parameters on the predicted wedge shape, based on the simple analysis discussed above. We examined a number of models to determine whether the results conformed to our expectations. Cases that failed to verify our first-order physical predictions are indicated in Table B1a.

Parameters Affecting Decollement Strength

The first group of parameters are those that directly affect the frictional or ductile strength of the decollement. Parameters that are positively correlated with the frictional strength tend to decrease the width of zone II and increase the frictional taper and the maximum taper. As an example, Figures B1a and B1b show the effects of the product $\mu_d(1-\lambda_d)$ on predicted topography and surface slope, respectively. As expected, larger values result in steeper surface slopes and narrower steep slope regions. Figures

B1a and B1b also indicate that increasing the magnitude of the product $\mu_d(1 - \lambda_d)$ decreases the width of zone I. This behavior would not be predicted from our simple technique of looking at the direct effect of each parameter on the strengths of the wedge base and the decollement; however, there is an indirect effect due to the dependence of wedge taper on decollement strength (see equations (4) and (A33)). An increase in the frictional strength of the decollement causes the wedge thickness to increase more rapidly with distance from the toe, and the brittle-ductile transition in the wedge base thus occurs closer to the toe. Parameters that are positively correlated with the ductile strength of the decollement tend to increase both the width of the steeply sloping region and the maximum taper. Thus an increase in either the preexponential factor $s_d^{P_d}/\delta A_d$ or the activation energy Q_d would increase the magnitude of these two wedge characteristics.

Parameters Affecting Wedge Base Strength

Parameters that are positively correlated with an increase in the brittle strength of the wedge base tend to increase the width of zone II and decrease the brittle-frictional taper. We might expect that increases in these parameters would decrease the width of zone I; however, increases in either C_h or $(1-\lambda_h)\sin\phi_h/(1-\sin\phi_h)$ also result in a narrower frictional taper, thus pushing the wedge base transition farther from the toe. An increase in the generalized viscosity coefficient A of the wedge material causes the ductile strength of the wedge base to decrease, resulting in a decrease in the width of zone I and an increase in the width of zone II and the maximum taper. Increasing the wedge activation energy decreases the ductile strength of the wedge, resulting in an increase in the width of zone I, a decrease in the width of zone II, and a decrease in the maximum taper (Figure B2). Larger values of activation energy also result in a slightly smaller brittle-frictional wedge taper, although this is not reflected in the surface slopes of Figure B2b. In this particular case, the flexural response of the underlying elastic layer has obscured some of the details of the wedge geometry. Another interesting feature observed in Figure B2 is the absence of a steep slope region for an activation energy of 165 kJ/mol. In this case, the brittle-ductile transition within the decollement zone occurs at a shallower depth than it does within the wedge base, as seen in Figure B2c. As a result, the wedge taper decreases sharply beyond the decollement frictional-ductile transition (see Figure B2b). As mentioned in the model characteristics section, this type of wedge morphology may occur under certain circumstances, but in this study we have chosen to focus on the type of morphology typified by Figure 1.

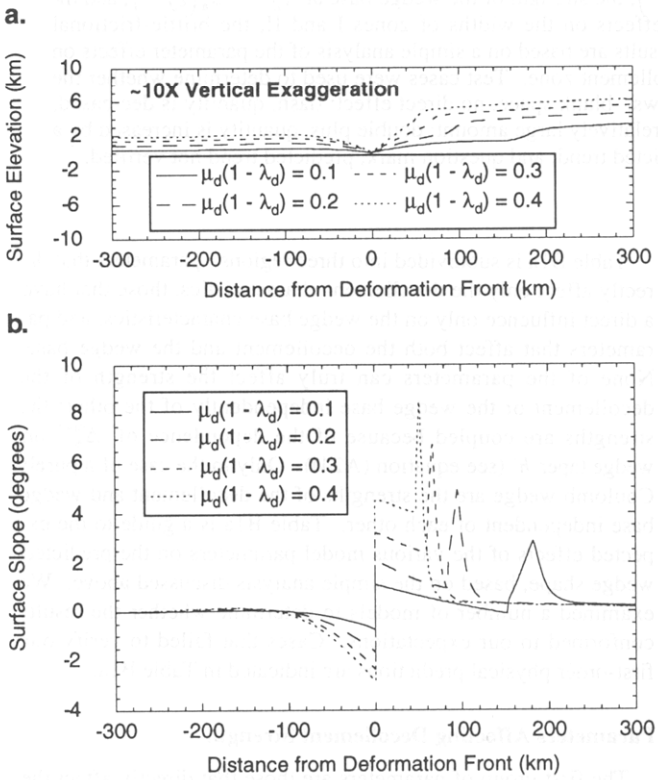

Figure B1. Effects of decollement frictional properties on predicted wedge shape. (a) Predicted surface topography for several different values of the product $\mu_d(1 - \lambda_d)$. (b) Predicted surface slopes for the same product values. Higher values result in steeper surface slopes and narrower regions of steep slope. Higher values also move the steep slope region closer to the toe of the wedge.

Parameters Affecting the Decollement and the Wedge Base

The thickness of the incoming wedge material h_0 and the relative velocity across the decollement zone u_0 are both related to the strain rate within the wedge and the decollement zone. Larger values for h_0 imply higher strain rates within the wedge (see equation (A23)), thus increasing the ductile strength of the wedge material. Within the decollement zone, h_0 is negatively correlated with strain rate (see equation (A27)), causing a decrease in the ductile strength of the decollement. The net result of increasing h_0 is a decrease in the width of zone II and in the maximum wedge taper. The convergence velocity u_0 affects the strain rates in both the wedge base and the decollement in the same way, but the effect on the ductile strength is likely to be greater for the decollement zone due to the differences in the assumed ductile deformation mechanisms. The ductile strength is proportional to $u_0^{1/n}$, where n is the power law exponent (see equations (A24) and (A28)). Thus the effect will be greater within the decollement zone, where $n = 1$ (diffusion flow), than within the wedge, where n is typically 2 or greater (dislocation creep). The net effect of an increase in the convergence velocity is an increase in the width of zone I and a decrease in the brittle-frictional taper. In test cases, the observable quantities were not found to be particularly sensitive to variations in the convergence velocity.

The density of the wedge material ρ_c affects the frictional strength of both the wedge base and the decollement. For a purely brittle-frictional wedge, the density provides a length scale for the cohesive problem. Length scales arise when the uniaxial compressive strength in the wedge base C_h and the cohesion of the decollement S_d are divided by the product $\rho_c g$ (see equations (A13), (A15), and (A16)). If $C_h = S_d = 0$, the problem has no natural length scale, as was found by *Dahlen* [1984] for a noncohesive wedge. In our case, the problem has a length scale even in the absence of cohesion due to the inclusion of ductile behavior. Increasing the density will cause the Coulomb-ductile transition to occur at a shallower depth for both the wedge base and the decollement zone. The effect will generally be greater for the decollement zone, however, since the frictional strength of the decollement is always less than or equal to the strength of the wedge base (see Figure 7c). An increase in the wedge density will thus produce decreases in the widths of zones I and II and increases in the brittle-frictional taper and the maximum taper.

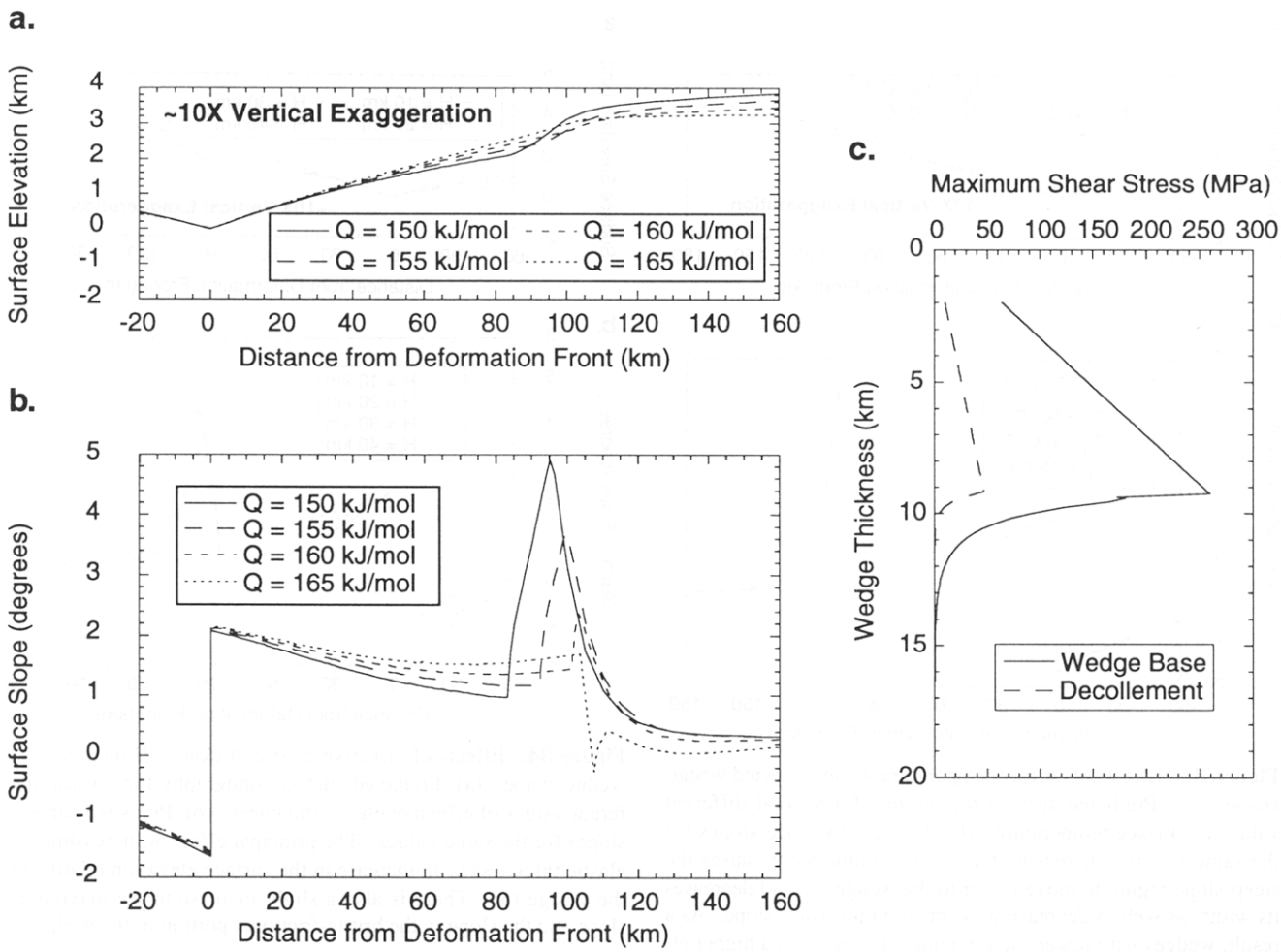

Figure B2. Effects of wedge activation energy Q on predicted wedge shape. (a) Predicted surface topography for several different values of wedge activation energy. (b) Predicted surface slopes for the same values. Larger values move the steep slope region further from the wedge toe, decrease the width of the steep slope region, and decrease the maximum surface slope. Larger values also slightly increase the slope in the brittle-frictional portion of the wedge, although the wedge taper in this region actually decreases with increasing values of activation energy. (c) Predicted strengths of the wedge base and decollement zone for an activation energy of 165 kJ/mol. In this case the decollement brittle-ductile transition occurs at a shallower depth than the wedge transition. The result is a sharp decrease in the wedge surface slope rather than the increase that is normally observed.

Another set of parameters affecting wedge shape are those related to temperature. Increasing either the surface temperature at the wedge toe T_0 or the planetary thermal gradient ∇T will move the Coulomb-ductile transitions closer to the surface (see equations (A18) and (A19)). An increase in the atmospheric temperature gradient ∇T_A will have the opposite effect. The exponential temperature dependence is controlled by the ratio Q_h/n for the wedge base and by the ratio Q_d/n_d for the decollement (see equations (A24), (A25), (A28), and (A29)). Since ductile deformation within the decollement is controlled by diffusion flow ($n \approx 1$), whereas ductile deformation within the wedge base is controlled primarily by dislocation creep ($n \approx 2$ or greater), the ratio Q_d/n_d will generally be larger than the ratio Q_h/n, if Q_d and Q_h are of comparable magnitudes. For that reason, the thermal environment will generally have a larger effect on the strength of the decollement than it will on the strength of the wedge base. This also implies that decollement strength will generally fall off more rapidly with increasing temperature than will the strength of the wedge base. Thus, by equation (4), the wedge taper will decrease very rapidly below the decollement frictional-ductile transition, yielding the relatively flat plateau of our model. Increasing the surface temperature or the planetary thermal gradient will have the effect of decreasing the width of zones I and II, as well as decreasing the maximum wedge taper, as shown in Figures B3a and B3b. Increasing the atmospheric temperature gradient will have the opposite effect. The net result of increasing the surface temperature is a decrease in the maximum elevation at the wedge crest. Once again, there is a case (T_0 = 150°C) where the decollement transition occurs at a shallower depth than the wedge base transition. Since the decollement is nowhere able to sustain significant amounts of shear stress, little topography is generated.

Parameters Related to Flexural Isostasy

Thus far, we have only examined the parameters affecting the strengths of the decollement and the wedge base; however, parameters affecting the flexural isostatic response of the elastic layer will also influence the observed wedge shape. One impor-

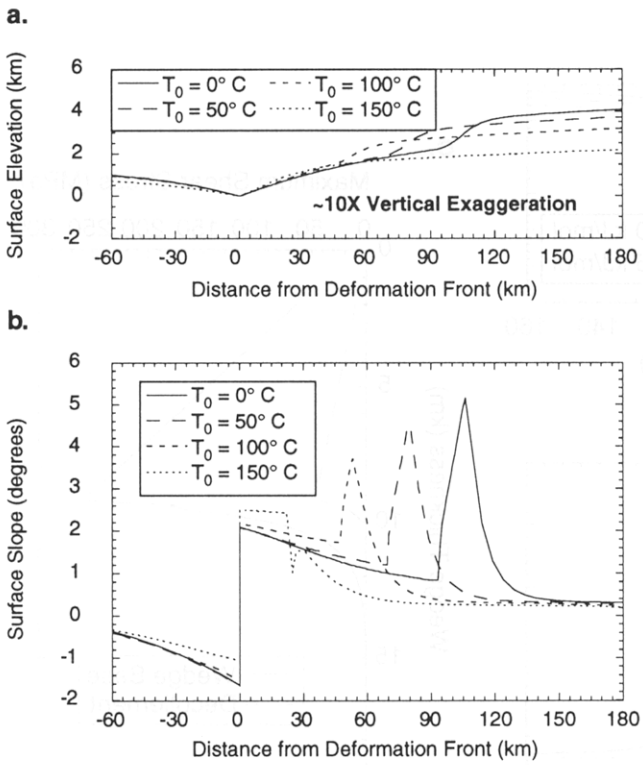

Figure B3. Effects of surface temperature T_0 on predicted wedge shape. (a) Predicted surface topography for several different values of surface temperature. (b) Predicted surface slopes for the same values. Increasing the surface temperature causes the steep-slope region to move closer to the wedge toe and decreases its width, as well as decreasing the maximum surface slope. As a result, wedges with lower surface temperatures attain a higher elevation. For a surface temperature of 150°C, the decollement frictional-ductile transition occurs at a shallower depth than the wedge base transition, resulting in a wedge with little topography.

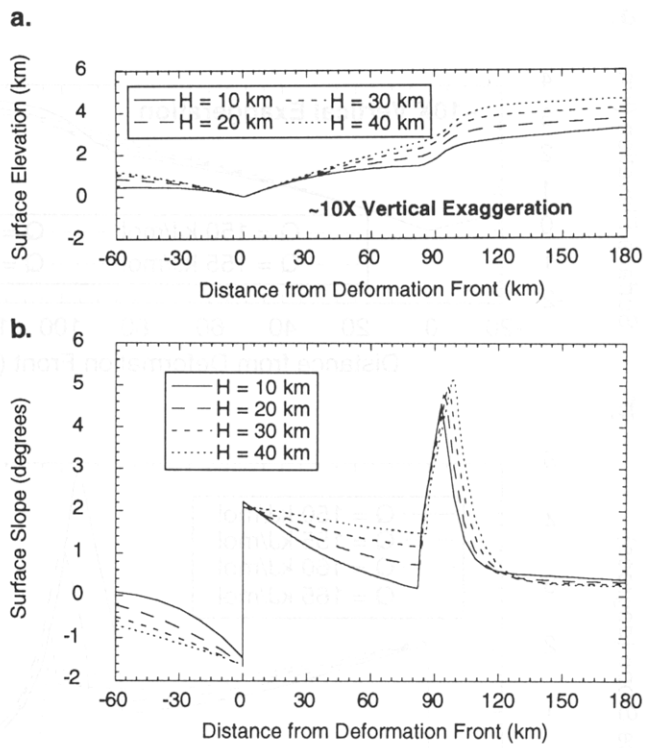

Figure B4. Effects of effective elastic thickness H on predicted wedge shape. (a) Predicted surface topography for several different values of effective elastic thickness. (b) Predicted surface slopes for the same values. The principal effect of increasing the elastic thickness is an increase in the surface elevation relative to the wedge toe. There is also a slight increase in the maximum slope and the slope in the brittle-frictional portion of the wedge.

tant parameter is the density contrast between the wedge material and the underlying mantle (see equations (A45) and (A46)). The larger the density contrast, the greater the amount and the steepness of topography that can be supported. A second set of parameters affecting wedge geometry are those affecting the flexural response of the elastic layer to an applied load. This set of parameters includes the Young's modulus E, Poisson's ratio ν, and the effective elastic thickness H. By far the most important of these is the elastic thickness, since the flexural rigidity is proportional to H^3 (equation (A40)). An increase in the elastic thickness decreases the amount of flexure in the plate, distributing the load of the wedge over a larger area. A more rigid plate is able to support greater amounts of relief and steeper surface slopes. As described previously, we should attach no particular physical significance to the value of the elastic thickness. It is simply a convenient means of quantifying the average strength of the lithosphere over geologic timescales. The influence of the effective elastic thickness on wedge topography is seen in Figures B4a and B4b, which show the surface elevations and surface slopes for different values of H. The effect on the maximum surface slope is not particularly significant: the difference in surface slope between H = 10 km and H = 40 km is only about 1 degree. The primary effect is an increase in the overall wedge elevation.

We would expect the effective elastic thickness to be related to the planetary thermal environment: lower surface temperatures and thermal gradients should yield a thicker elastic layer. Such a correlation could have been explicitly included in our model, such that H is determined by specifying T_0 and ∇T. For a given T_0, the elastic thickness would be approximately inversely proportional to ∇T. We have not done this, both because of the preliminary nature of this study, and because the actual correlation between thermal gradient and elastic thickness may be much more complicated. *Molnar and Lyon-Caen* [1988] have pointed out, for example, that differences of 10^3 times in the estimated flexural rigidities for plates beneath India and the Adriatic Sea would imply a factor of 10 difference in the geothermal gradients, an unlikely situation. Thus, for our analysis, we assume that temperature and the elastic thickness are negatively correlated, but we do not quantify the relationship between them. This relationship will significantly affect the predicted wedge topography. Lower surface temperatures and/or thermal gradients result in steeper maximum surface slopes and greater wedge topography, as do increases in the effective elastic thickness. These effects will therefore reinforce each other. This behavior has important implications for the geometry of accretionary wedges on Venus, where the thermal environment is likely to play an important role.

Acknowledgments. This work was supported by NSF grant EAR-9104477. We would like to thank Bryan Isacks for the use of his South American digital topographic data set and Jan Tullis for helpful discussions on rheology. This manuscript benefited from thoughtful reviews by Sean Willett, Norm Sleep, and an anonymous reviewer. Work performed under the auspices of the U.S. Department of Energy by the Lawrence Livermore National Laboratory under contract W-7405-ENG-48.

References

Allmendinger, R. W., V. A. Ramos, T. E. Jordan, M. Palma, and B. L. Isacks, Paleogeography and Andean structural geometry, Northwest Argentina, *Tectonics*, *2*, 1-16, 1983.

Byerlee, J. D., Friction of rocks, *Pure Appl. Geophys.*, *116*, 615-626, 1978.

Chapman, D. S., Thermal gradients in the continental crust, in The Nature of the Lower Continental Crust, edited by J. B. Dawson, D. A. Carswell, J. Hall, and K. H. Wedepohl, *Spec. Publ. Geol. Soc. Am.*, *24*, 63-70, 1986.

Chapple, W. M., Mechanics of thin-skinned fold-and-thrust belts, *Geol. Soc. Am. Bull.*, *89*, 1189-1198, 1978.

Dahlen, F. A., Noncohesive critical Coulomb wedges: An exact solution, *J. Geophys. Res.*, *89*, 10,125-10,133, 1984.

Dahlen, F. A., Critical taper model of fold-and-thrust belts and accretionary wedges, *Annu. Rev. Earth Planet. Sci.*, *18*, 55-99, 1990.

Davis, D., J. Suppe, and F. A. Dahlen, Mechanics of fold-and-thrust belts and accretionary wedges, *J. Geophys. Res.*, *88*, 1153-1172, 1983.

Elliott, D., The motion of thrust sheets, *J. Geophys. Res.*, *81*, 949-963, 1976.

Emmerman, S. H., and D. L. Turcotte, A fluid model for the shape of accretionary wedges, *Earth Planet. Sci. Lett.*, *63*, 379-384, 1983.

Evans, B., and G. Dresen, Deformation of Earth materials: Six easy pieces, *U.S. Nat. Rep. Int. Union Geod. Geophys. 1987-1990*, *Rev. Geophys.*, *29*, 823-843, 1991.

Fielding, E., B. Isacks, M. Barazangi, and C. Duncan, How flat is Tibet?, *Geology*, *22*, 163-167, 1994.

Gradshteyn, I. S., and I. M. Ryzhik, *Table of Integrals, Series, and Products*, 1160 pp., Academic, San Diego, Calif., 1980.

Head, J. W., Formation of mountain belts on Venus: Evidence for large-scale convergence, underthrusting, and crustal imbrication in Freyja Montes, Ishtar Terra, *Geology*, *18*, 99-102, 1990.

Hubbert, M. K., and W. W. Rubey, Role of fluid pressure in mechanics of overthrust faulting, 1, Mechanics of fluid-filled porous solids and its application to overthrust faulting, *Geol. Soc. Am. Bull.*, *70*, 115-166, 1959.

Isacks, B. L., Uplift of the central Andean plateau and bending of the Bolivian orocline, *J. Geophys. Res.*, *93*, 3211-3231, 1988.

Jaeger, J. C., and N. G. W. Cook, *Fundamentals of Rock Mechanics*, 593 pp., Chapman and Hall, New York, 1979.

Karato, S., M. S. Paterson, and J. D. Fitzgerald, Rheology of synthetic olivine aggregates: Influence of grain size and water, *J. Geophys. Res.*, *91*, 8151-8176, 1986.

Kaula, W. M., Venus: A contrast in evolution to Earth, *Science*, *247*, 1191-1196, 1990.

Kerr, R. A., Did Venus hiccup or just run down?, *Science*, *259*, 1400-1401, 1993.

Kerr, R. A., A new portrait of Venus: Thick-skinned and decrepit, *Science*, *263*, 759-760, 1994.

Kirby, S. H., Rheology of the lithosphere, *Rev. Geophys.*, *21*, 1458-1487, 1983.

Kirby, S. H., and A. K. Kronenberg, Rheology of the lithosphere: Selected topics, *Rev. Geophys.*, *25*, 1219-1244, 1987. (Correction, *Rev. Geophys.*, *25*, 1680-1681, 1987.)

Kliore, A. J., V. I. Moroz, and G. M. Keating, The Venus international reference atmosphere, *Adv. Space Res.*, *5*(11), 25-29, 1985.

LePichon, X., M. Fournier, and L. Jolivet, Kinematics, topography, shortening, and extrusion in the India-Eurasia collision, *Tectonics*, *11*, 1085-1098, 1992.

Lyon-Caen, H., P. Molnar, and G. Suárez, Gravity anomalies and flexure of the Brazilian shield beneath the Bolivian Andes, *Earth Planet. Sci. Lett.*, *75*, 81-92, 1985.

Lyons, D. T., Magellan planetary constants and models, *JPL Publ., JPL D-2300, Rev. D.*, 1991.

McNamee, J. B., N. J. Borderies, and W. L. Sjogren, Venus: Global gravity and topography, *J. Geophys. Res.*, *98*, 9113-9128, 1993.

Mingramm, A., A. Russo, A. Pozzo, and L. Cazau, Sierras Subandianas, in *Segundo Simposio de Geologia Regional Argentina*, vol. 1, pp. 95-138, Academia Nacional de Ciencias, Cordoba, Argentina, 1979.

Molnar, P., and P. England, Late Cenozoic uplift of mountain ranges and global climate change: Chicken or egg?, *Nature*, *346*, 29-34, 1990.

Molnar, P., and H. Lyon-Caen, Some simple physical aspects of the support, structure, and evolution of mountain belts, *Spec. Pap. Geol. Soc. Am.*, *218*, 179-207, 1988.

Moran, J. M., and M. D. Morgan, *Meteorology: The Atmosphere and the Science of Weather*, Macmillan, New York, 1991.

Oxburgh, E. R., Heat flow and magma genesis, in *Physics of Magmatic Processes*, edited by R. B. Hargraves, pp. 161-199, Princeton University Press, Princeton, N. J., 1980.

Paterson, M. S., Problems in the extrapolation of laboratory rheological data, *Tectonophysics*, *133*, 33-43, 1987.

Price, E. J., C. Connors, F. A. Dahlen, J. Suppe, and C. A. Williams, Accretionary wedge mechanics on Venus: A brittle/ductile critical taper model (abstract), *Lunar Planet. Sci.*, *23*, 1105-1106, 1992.

Rutter, E. H., and K. H. Brodie, The role of tectonic grain size reduction in the rheological stratification of the lithosphere, *Geol. Rundsch.*, *77*, 295-308, 1988.

Rutter, E. H., and K. H. Brodie, Lithosphere rheology—A note of caution, *J. Struct. Geol.*, *13*, 363-367, 1991.

Salvador, M., and J. N. Kellogg, Gravity field, crustal structure and effective elastic thickness of the North Andes (abstract), *Eos Trans. AGU*, *72* (17), Spring Meeting suppl., 91, 1991.

Sandwell, D. T., and G. Schubert, Flexural ridges, trenches, and outer rises around coronae on Venus, *J. Geophys. Res.*, *97*, 16,069-16,083, 1992.

Shelton, G., and J. Tullis, Experimental flow laws for crustal rocks (abstract), *Eos Trans. AGU*, *62*, 396, 1981.

Solomon, S. C., Keeping that youthful look, *Nature*, *361*, 114-115, 1993.

Solomon, S. C., and J. W. Head, Lithospheric flexure beneath the Freyja Montes foredeep, Venus: Constraints on lithospheric thermal gradient and heat flow, *Geophys. Res. Lett.*, *17*, 1393-1396, 1990.

Stockmal, G. S., Modeling of large-scale accretionary wedge formation, *J. Geophys. Res.*, *88*, 8271-8287, 1983.

Strehlau, J., and R. Meissner, Estimation of crustal viscosities and shear stresses from an extrapolation of experimental steady state flow data, in *Composition, Structure and Dynamics of the Lithosphere-Asthenosphere System*, *Geodyn. Ser.*, vol. 16, edited by K. Fuchs and C. Froidevaux, pp. 69-87, AGU, Washington, D.C., 1987.

Suppe, J., and C. Connors, Critical taper wedge mechanics of fold-and-thrust belts on Venus: Initial results from Magellan, *J. Geophys. Res.*, *97*, 13,545-13,561, 1992.

Surkov, Y. A., L. P. Moskalyeva, O. P. Scheglov, V. P. Kharyukova, O. S. Manvelyan, V. S. Kirichenko, and A. D. Dudin, Determinations of the elemental composition of rocks on Venus by Venera 13 and Venera 14 (preliminary results), *Proc. Lunar Planet. Sci. Conf. 13th*, part 2, *J. Geophys. Res.*, *88*, suppl., A481-A493, 1983.

Tullis, J., and R. A. Yund, Dynamic recrystallization of feldspar: A mechanism for ductile shear zone formation, *Geology*, *13*, 238-241, 1985.

Tullis, J., and R. A. Yund, Diffusion creep in feldspar aggregates: Experimental evidence, *J. Struct. Geol.*, *13*, 987-1000, 1991.

Turcotte, D. L., An episodic hypothesis for Venusian tectonics, *J. Geophys. Res.*, *98*, 17,061-17,068, 1993.

Turcotte, D. L. and G. Schubert, *Geodynamics Applications of Continuum Physics to Geological Problems*, 450 pp., John Wiley, New York, 1982.

Vorder Bruegge, R. W., and R. C. Fletcher, A model for the shape of overthrust zones on Venus (abstract), *Lunar Planet. Sci.*, *21*, 1278-1279, 1990.

Wang, K., R. D. Hyndman, and E. E. Davis, Thermal effects of sediment thickening and fluid expulsion in accretionary prisms: Model and parameter analysis, *J. Geophys. Res.*, *98*, 9975-9984, 1993.

Wang, W. H. and D. M. Davis, Sandbox model simulation of forearc evolution (abstract), *Eos Trans. AGU*, *73* (14), Spring Meeting suppl., 293-294, 1992.

Willett, S. D., Dynamic and kinematic growth and change of a Coulomb wedge, *Thrust Tectonics*, edited by K. R. McClay, pp. 19-31, Chapman and Hall, New York, 1992.

Willett, S., C. Beaumont, and P. Fullsack, Mechanical model for the

tectonics of doubly vergent compressional orogens, *Geology*, *21*, 371-374, 1993.

C. Connors, F. A. Dahlen, and J. Suppe, Department of Geological and Geophysical Sciences, Princeton University, Princeton, NJ 08544. (e-mail: chris@wanda.princeton.edu; tony@wobbly.princeton.edu; john@wanda.princeton.edu)

E. J. Price, Scripps Institute of Oceanography, University of California, San Diego, IGPP 0225, La Jolla, CA 92093. (e-mail: evelyn@mahi.ucsd.edu)

C. A. Williams, Lawrence Livermore National Laboratory, L-202, Livermore, CA 94550. (e-mail: cwilliams@llnl.gov)

(Received November 22, 1993; revised April 25, 1994; accepted May 18, 1994.)